Development, Characterization, and Applications of a 3D Printed micro Free-Flow Electrophoresis Device

A DISSERTATION SUBMITTED TO THE FACULTY OF THE UNIVERSITY OF MINNESOTA BY

Sarah Kate Anciaux

IN PARTIAL FULFILLMENT OF THE REQUIREMENTS FOR THE DEGREE OF DOCTOR OF PHILOSOPHY

Michael T. Bowser, Advisor

February 2017

Acknowledgements

Ever since my first real science class in 7th grade I have known that I love the sciences and learning new things. Without the enthusiasm, support, and encouragement of my teachers, professors, family, and friends, I would not have been able to accomplish and learn all that I have.

I would like to start by thanking Mark Kluber, my middl school science teacher that showed me how fun and cool it was to understand what was going on in the world on a scientific level. His enthusiasm is what got me to fall in love with learning and science in general.

I would also like to thank Bruce Wilson, my high school chemistry teacher. His love of chemistry and horribly amazing chemistry jokes are what led me to love chemistry the most. His dedication to his students, and pure love of the subject matter encouraged me to continue studying chemistry.

My professors Maria Dean and Marty St Clair were also huge influences on me during my undergraduate career. They always pushed me to achieve the most, and get the most out of my liberal arts education. Their dedication to their students, and desire to help them become the best people and students they can be was unwavering. They helped me to get in a position where I could not only get into graduate school, but also be very successful there.

I also thank Mike Bowser, my graduate advisor. Joining his research group was one of the best decisions I made during my graduate career. His guidance and encouragement have helped me get through the highs and lows of graduate school, and to help me develop all of the skills that I have today.

Furthermore, the other group members Mike has brought in have been encouraging and helpful with discussions and assistance. Specifically Matt Geiger, Alex Johnson, Kailey Soller, Megan Weisenberger, and Rachel Harstad have been understanding and helpful throughout my career.

I would like to thank my parents Don and May Anciaux. They have always been so supportive and encouraging. If it weren't for them pushing me to get good grades, play every sport, and take in everything I could when I was younger, I know I wouldn't have been as successful as I am today.

Finally, I would like to thank my wife, Patty King. We met at the start of my graduate career, and I know that it would not have been the same without her support.

Dedicated to my parents, Don and May Anciaux, and my wife, Patty King.

Abstract

Micro free-flow electrophoresis (μFFE) is a unique separation technique because of its continuous nature. Analytes are pressure driven through a planar separation channel, and an electric field applied laterally to the flow producing a spatial separation. Fabrication methods associated with μFFE devices hinder our ability to address the limitations of μFFE. This work focuses on a novel fabrication method to reduce the overall fabrication cost and time, followed by validating and characterizing the device. A novel μFFE device is fabricated in acrylonitrile butadiene styrene (ABS) by 3D printing two sides of the device and then acetone vapor bonding them while simultaneously inserting electrodes and clarifying the device. Fluorescent dyes are separated, and their limit of detection determined. After validation of the new fabrication method, a new device design is made with the sample inlet modified so that 2D nLC × μFFE separations can be performed. 2D nLC × μFFE separations of fluorescent dyes, proteins, and tryptic BSA digest are demonstrated. These samples allow comparison between the surface properties of glass and 3D printed devices. Peak asymmetries, widths, and the interface were investigated. Minimal surface adsorption is observed for fluorescent dyes, proteins, and peptides, unlike in glass devices. After investigating surface properties, an open edge device for coupling to mass spectrometry is designed and compared to its glass counterpart. A novel ionization method is demonstrated from a hydrophobic membrane and the open edge device is shown to have stable flow.

Table of Contents

List of Tables

List of Figures

List of Abbreviations

µFFE	Micro free-flow electrophoresis
µFFIEF	Micro free-flow isoelectric focusing
2D	Two-dimensional
3D	Three-dimensional
ABS	Acrylonitrile Butadiene Styrene
aSi	Amorphous silicon
CCD	Charge coupled device
CE	Capillary electrophoresis
CNC	Computer numerical control
DNA	Deoxyribose nucleic acid
FDM	Fused Deposition Modeling
FFE	Free-flow electrophoresis
HPLC	High performance liquid chromatography
IEF	Isoelectric focusing
ITP	Isotachophoresis
LC	Liquid chromatography
LIF	Laser induced fluorescence
m/z	Mass-to-charge ratio
MALDI	Matrix assisted laser desorption ionization
MEKC	Micellar electrokinetic chromatography
MS	Mass Spectrometry

nLC	Nano-liquid chromatography
PDMS	Polydimethylsiloxane
PVDF	Polyvinylidene difluoride
RIE	Reactive ion etching
TOF	Time of Flight
ZE	Zone electrophoresis

Chapter 1

Introduction

1.1 Free-Flow Electrophoresis

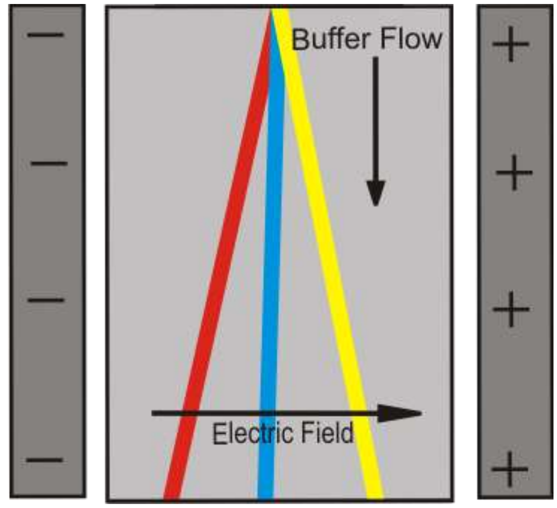

Figure 1.1. Diagram of FFE as a sample is introduced into a planar separation channel. Analytes are then separated based on their electrophoretic mobility as a voltage is applied laterally to the buffer flow.

Electrophoresis is a common separation technique in biochemistry for its ability to separate deoxyribose nucleic acid (DNA), peptides, proteins, and cells. Free-flow electrophoresis (FFE) was first introduced on a large scale in the early 1960s.[1,2] In this technique, buffer is pressure-driven through a planar separation channel and the sample introduced in-stream. The application of an electric field perpendicular to the separation channel, shown in Figure 1.1, causes charged analytes to deflect laterally based on their electrophoretic mobility. The deflection distance depends on analyte charge, solution viscosity, and analyte ionic radius. FFE has been used for proteomics and more commonly for separations of cells and their components.[3-5]

Frequently FFE has been used as a preparative scale separation technique, used for pre-sorting and concentration with 25 mL separation channels. Due to the large nature of the separation channel and low surface-area-to-volume ratio, heat dissipation is low and heat generation high, leading to Joule heating. The large amount of Joule heating ultimately limits the electric field that can be applied, reducing the resolution of the separation, or causing breakdown of the device material.[6]

1.1.1 Miniaturization of Free-Flow Electrophoresis

Raymond *et al.* were the first to produce a silicon microscale FFE device in 1994.[7,8] Since this first attempt at μFFE many groups have continued to develop and improve μFFE devices by fabricating in substrates that allow for higher voltages to be applied such as polydimethylsiloxane (PDMS), Pyrex ® and glass (see Figure 1.2).[9-12]

Miniaturizing the FFE device increased the surface-area-to-volume ratio 20-50 times compared to preparative scale FFE, greatly increasing heat dissipation and resolution.[13] This decrease in Joule heating allows greater voltages to be applied.[14,15] In addition to increasing separation efficiency, the smaller devices can achieve separations in much shorter time periods.[10,16] The micro scale also allows for use of smaller reagent and sample volumes producing less waste.

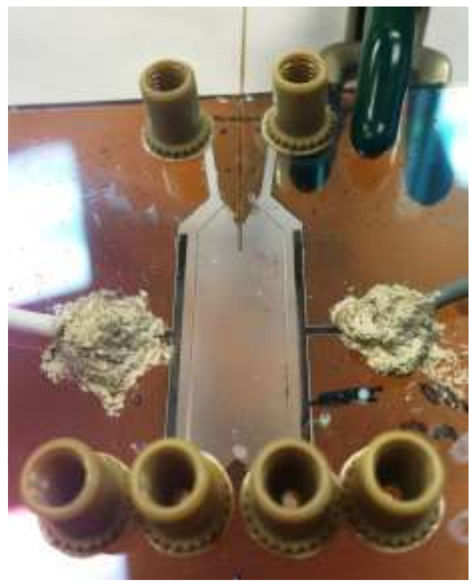

Figure 1.2. Miniaturized free flow electrophoresis device.

Originally upon miniaturization of FFE some problems were seen such as electrolysis bubbles interfering with the separation and poor stream stability.[17] After many attempts at resolving these problems,[15] the integration of deeper electrode channels and addition of a surfactant to the running buffer has greatly reduced problems due to electrolysis products.[11,17] Deeper electrode channels of

~80 μm compared to the ~20 μm separation channels allow for faster flow rates over the electrodes, removing the electrolysis products before they can interfere with the separation bed. This channel depth difference allows a slow flow rate in the separation channel to enhance the separation, and removal of electrolysis products. Buffer additives such as organic modifiers, and surfactants were shown to improve stream stability by reducing the surface tension and producing smaller bubbles.[18] Triton X-100 was shown to be the best at improving stream stability, with a 12-fold increase leading to long-term use > 2 hr.[17]

1.1.2 Spatial Broadening in μFFE

Fonslow and Bowser experimentally verified the parameters that contribute to the broadening in μFFE. They demonstrated that the spatial broadening in a μFFE device can be attributed to Equation 1.1:

$$\sigma_{total}^2 = \sigma_{inj}^2 + \sigma_D^2 + \sigma_{HD}^2 = \frac{w_{inj}^2}{12} + \frac{2DL}{v} + \frac{h^2 d^2 v}{105DL} \qquad (1.1)$$

Where (w_{inj}^2) is the width of the sample stream at the sample inlet, D is the analyte diffusion coefficient, L is the vertical distance between the sample inlet and detection zone, v is the linear velocity of the buffer, h is the height of the separation channel, and d is the distance the analyte is deflected in the electric field. The total variance of the analyte band (σ_{total}^2) is determined by the sum of the individual broadening source variances. This includes broadening from the initial stream width at injection (σ_{inj}^2), diffusion (σ_D^2), hydrodynamic diffusion (σ_{HD}^2). It was determined that hydrodynamic broadening governed broadening at high combinations of buffer velocity and electric fields while diffusion dominated at low flow rates.

1.1.3 Modes of Operation and Applications

Similar to its preparative scale counterpart, μFFE can be run in various modes including zone electrophoresis (ZE), micellar electrokinetic chromatography (MEKC),[18] isoelectric focusing (IEF),[19] and isotachophoresis (ITP).[20] Briefly, utilizing ZE, analytes are separated solely based on their electrophoretic mobility. By adding a surfactant to the buffer above its critical micellar concentration, MEKC can be performed and enables the separation of neutral analytes as they partition across the micelles. If instead of adding a surfactant, ampholytes are introduce for IEF the analytes will migrate until they reach their pI and have a net charge of zero where they no longer move in the electric field. ITP can be implemented by using a high ionic mobility and a low ionic mobility electrolyte buffers with the analytes of interest between the two buffers. Application of an electric field facilitates focusing of analytes at the trailing and leading electrolyte interface. By simply changing the buffer composition, the mode can be easily switched and different mechanisms utilized to achieve the separation. This ability to switch modes easily has made it a desirable technique for many applications.[21] Various modes of operations have been employed for numerous applications in μFFE. Separation of amino acids,[12,22-26] fluorescent dyes,[10,25-29] proteins,[19,24,26,30-33] organelles,[34-36] and whole cells have been reported.[34] Recent applications of μFFE include rapid optimization of separation conditions,[37] quantification of aptamer-protein binding[38], aptamer selections[39], and high peak capacity 2D separations.[40,41]

1.1.4 Detection and Identification Methods for μFFE

Laser induced fluorescence (LIF), Ultra Violet (UV), electrochemical, surface enhanced Raman scattering, and Fourier transform infrared detection methods have all been used in microfluidic devices.[42] Unfortunately, the continuous nature, planar separation channel, and small detection path length of μFFE devices makes it difficult to interface with many detection methods.[43] A common detection method for μFFE is LIF due to its sensitivity, selectivity, and ability to image over a space.[43] This technique utilizes a laser beam that has been focused into a line through optics. The laser line can then induce fluorescence of compatible samples in the separation channel that are imaged through a microscope and charge coupled device (CCD) camera. This is all done without the need for any scanning or moving parts during the separation.[43] Many analytes are not natively fluorescent so the addition of a sample derivatization step with a fluorescent molecule is often necessary with this technique. Even after derivatization and detection, the samples are detectable, but still unidentifiable with FFE. This occurs because migration distances do not necessarily correlate to molecular weight or any other unambiguously identifiable characteristic.

An important area of study in μFFE is the improvement in the detection and identification schemes used. The lack of identification with current detection methods limits the utility of μFFE for complex samples. Many other separation techniques, such as capillary electrophoresis (CE) and liquid chromatography (LC)[44,45] have been coupled to mass spectrometry resulting in much more powerful analysis. A more direct coupling of μFFE devices and mass spectrometry could lead to analysis and identification of more complex samples. Also the direct coupling could allow for simplified mass spectrometry database searches, as the pI of proteins could be known when IEF mode is used, leading to easier identification.[46] Commonly used mass spectrometric couplings include electrospray ionization or Matrix Assisted Laser Desorption ionization (MALDI) coupled to quadrupole or time of flight (TOF) identification,[47,48] which do not couple well to μFFE due to the separation taking place in space instead of time like most separation techniques.

1.2 Device Fabrication

1.2.1 Current Fabrication Methods

There are many well characterized manufacturing processes for fabricating microfluidic devices. These fabrication procedures were at first heavily influenced by technologies developed for microelectronic manufacturing.[49] The Bowser group was the first to use glass microfabrication to produce μFFE devices. The fabrication of a μFFE device is outlined in Figure 1.3. Briefly, borofloat glass wafers are first deposited with amorphous silicon (aSi) by plasma enhanced chemical vapor deposition. The aSi can then be patterned and etched using standard photolithography and reactive ion etching (RIE) techniques. The exposed glass is then etched to the desired depth using hydrofluoric acid. Repetition of the photolithography RIE and wet etching steps can be used to produced features of various depths on the same device. After successful production of the features in the glass, the remaining aSi can then be removed by RIE, and electrodes patterned. Electrodes are patterned using electron beam evaporation deposition of titanium and then gold. Photolithography and wet etching steps are repeated to remove the excess metal, leaving the electrodes

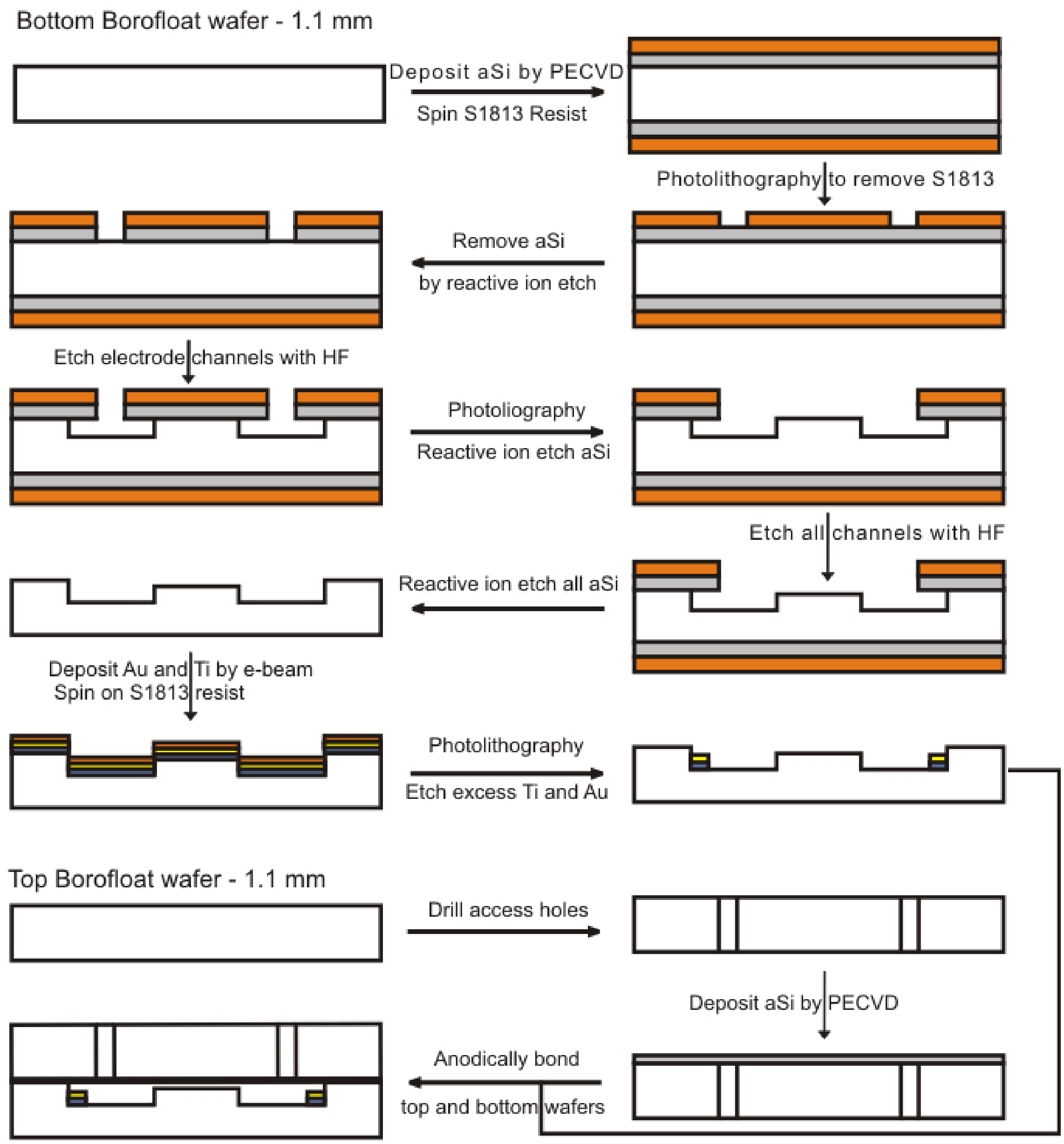

Figure 1.3. Schematic of glass device fabrication performed in a class 100 cleanroom.

patterned in the electrode channels of the glass device. Another blank glass wafer is then drilled by hand, producing fluidic access holes to align with the feature side device channels. This wafer is then cleaned and a thin layer of aSi deposited to facilitate anodic bonding of the feature side of the device and the fluidic access side. More detail of this procedure can be found in previous publications.[11,37,50] This process typically takes two weeks to complete and costs approximately $1000 per device if there are no major setbacks during production. Additional time would be required if new masks need created for a new design.

1.2.2 Recent Fabrication Methods for Micro-Free-Flow Electrophoresis

Driven by the large cost and difficulty of glass fabrication outlined in the previous section, polymer fabrication technology was introduced.[51] PDMS and other polymers saw a large increase in use due to their simplified fabrication processes and reduction in cost and time compared to glass fabrication methods. A large benefit of polymer fabrication was also the wide range of readily available materials allowing substrates to be chosen based on the chemical and physical properties that best fit the application.[51,52] There are two main workflow steps for polymer microfluidic manufacturing: master fabrication and photomask generation. Master fabrication includes hot embossing, casting, thermoforming, and injection molding. Photomask generation includes laser ablation and plasma etching.[52] Time, cost, available resources, and labor are factors in determining what manufacturing process to use when creating a microfluidic device.

In recent years, there has been a large push for one-step manufacturing processes and reductions in cost and time for microfluidics.[53] Recently μFFE devices have been fabricated faster and cheaper using these newly developed processes. For example, the use of laser printing toner as a substrate to fabricate μFFE devices with channels as shallow as 8 μm has been demonstrated by Pereira de Jesus *et al.*[54] Jezierski *et al.* used multistep liquid-phase lithography as a rapid prototyping strategy to produce μFFE devices in several hours.[25] Köhler *et al.* has demonstrated fabrication of μFFE by injection molding their devices. Walowski *et al.* used multi step lamination to produce low cost μFFE devices in a PMMA substrate in less than one hour.[55] Ding *et al.* used a photocurable polymer to bond etched glass wafers together to produce μFFE devices with reusable substrate layers.[56] Akagi *et al.* used masking tape to seal two computer numerical control (CNC) milled PMMA layers to fabricate a μFFE device.[57] These new fabrication methods suggest that mass production is feasible for μFFE devices.[58] All of these fabrication methods have either reduced the cost or the time consumed compared to glass fabrication, but many still require long annealing steps, master production, or costly specialized equipment.

1.2.3 3D Printing and Microfluidics

Three-dimensional (3D) printing, was first introduced in the mid-1980s[59] and is described as the use of metals, plastics, ceramics, composite, or biological materials to generate 3D objects layer by layer.[53,59,60] Since the 1980s, the use of 3D printing has rapidly expanded due to the ease of on-demand customization and personalization, reduction of waste, production of novel components, and ability to fabricate complex structures.[59] Some common 3D printing methods include fused deposition modeling (FDM), inkjet, powder, and stereolithography.[53,59,60] New 3D printing technologies are able to produce layers as thin as 1-100 μm, making fabrication of microfluidic devices feasible.[60]

With 3D printing, unlike other manufacturing processes, there is no need to produce a master prior to fabrication[53] and fluidic connections can be integrated directly into the device.[60,61] This decrease in cost, time, and labor dramatically decreases the design cycle time, enhancing the creative process of the user for developing new microfluidic applications. Some recent examples of 3D printed microfluidic devices include an FDM printed nanoparticle flow-injection amperometry device,[62] inkjet printing of multiple channels using commercial connections and inserts for drug transport studies,[61] and stereolithography to create an electrochemical flow cell with integrated electrodes.[63]

Fully enclosed microfluidic channels can be produced using a number of 3D printing strategies. Dual material printing can be used to introduce sacrificial layers, which can later be removed to expose the channel.[60,64] Direct 3D printing of open channels is possible, but challenging due to difficulty of fabricating an overhang without the support of a sacrificial layer.[53] Finally, enclosed channels can be sealed by bonding two thermoplastic parts together.[65] Bonding can be challenging if the plastic does not easily adhere to itself or another thermoplastic, or if small channels need to be aligning precisely. Gross *et al.* and Waldbaur *et al.* have compiled extensive comparisons of 3D printing methods and feature sizes.[53,60]

1.2.4 Fused Deposition Modeling (FDM)

In FDM, a hot end heats a polymer filament above its glass transition temperature as it is fed into a nozzle (see Figure 1.4). The heated material is then extruded from the nozzle and deposited onto a flat heated bed in a precise pattern using X/Y motors to control position. Another motor is used to control the rate of the filament insertion and deposition. After the pattern for one layer has been deposited, the stage is lowered by a set layer height, allowing further layers to be deposited along the Z axis. The polymer fuses to the previous layer as it is extruded creating a uniform material.

FDM offers a number of benefits over competing 3D printing technologies. FDM is compatible with a number of readily available thermoplastic polymers. Other 3D printing techniques require specific modified polymers, often proprietary blends that are expensive compared to more common thermoplastics. Drawbacks of FDM include rough surfaces produced by the tracking of the nozzle as the thermoplastic is extruded and lower resolution in the Z dimension.

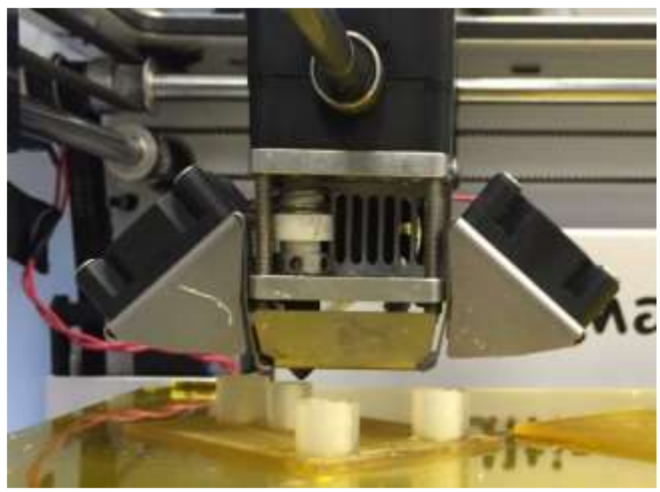

Figure 1.4. Picture of the fused deposition modeling (FDM) 3D printing head. A ABS filament is fed into a heated nozzle which extrudes the polymer in a pre-defined pattern. Once the pattern is complete the stage is lowered by the layer depth and a new layer can be deposited.

Fully enclosed channels can be fabricated with current FDM methods using dual extrusion heads to create sacrificial layers or using a solvent/polymer mixture to bond 3D printed parts together.[66] Solvent/polymer bonding relies on the solubility of the polymers in organic solvents. For ABS filament, acetone is used to dissolve a superficial layer of the part and the parts are fused by pressing them together. When the substrate layers are pressed together the partially dissolved polymer chains entangle and create a strong bond across the parts.[66] Liquid phase solvents are typically used to bond FDM parts together, but this method can leave brush marks where the solvent is applied. Dipping substrates directly into the solvent or vapor phase application can reduce these marks. Vapor phase application allows more precise control of solvent exposure to the polymer surface.[67]

FDM is the most easily accessible 3D printing technology available at this time.[68-76] Inexpensive, direct to consumer FDM printers are readily available. FDM is also compatible with inexpensive, widely available thermoplastic substrates.

1.2.5 μFFE Interface

Many improvements have been made in respect to the sample introduction and interface to μFFE devices over the last few years. Previously sample was introduced through the top of the device, perpendicular to the separation channel and buffer flow, show in Figure 1.5. This method utilized a Nanoport and a drilled access hole to directly

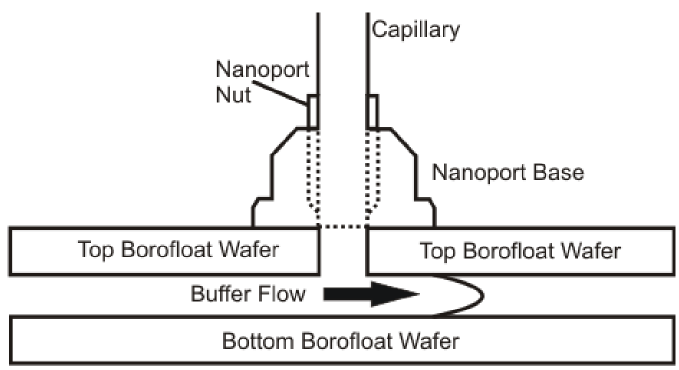

Figure 1.5. Diagram of sample interface entering μFFE separation channel from the top side of the device, perpendicular to buffer flow. The dead volume created by this interface can be seen between the buffer flow in the separation channel and the end of the dotted line associated with the capillary.

inject the sample utilizing a syringe pump. There were many issues with this method. Most notable was the significant amount of dead volume associated with the interface, which leads to mixing and loss of peak capacity when coupled to another separation technique. To overcome this issue, Geiger *et al.* developed a sample introduction technique that utilized a capillary to introduce sample into the separation channel through the side of the device, shown in Figure 1.6.[40] Sample can then be introduced directly from the capillary into the separation channel, parallel to the buffer flow. This eliminated the dead volume associated with the previous method and made 2D separations possible by improving the interface efficiency and reducing the dead volume mixing and loss of peak capacity attributed to the previous interface methods.

Figure 1.6. Glass fabricated µFFE device with the capillary inserted through the side of the device, parallel to buffer flow. Minimal dead volume is associated with this method.

1.2.6 Temporal Broadening and the Effect of Surface Adsorption in µFFE

Many temporal separation techniques can be effected by surface adsorption and require the addition of harsh chemicals to the buffer, or time consuming surface coating techniques. This type of broadening can result in poor peak symmetry, low resolution, and reduced peak capacities in 2D separations. For that reason, elimination of surface adsorption is necessary and should be investigated. Temporal broadening can be detrimental to a separation and depends on how strongly analytes interact with the channel surface. Stronger interactions result in analytes that are less likely to dissociate from the wall, and therefore broaden peaks and can even delay elution times. Many studies have been done on peak broadening, elution time delays, and electro-osmotic flow to characterize the effect of surface adsorption.[77-79] Means to remediate broadening due to surface adsorption have been employed, such as applying surface coatings to channels, or using buffers additives to limit the interactions between analytes and surface.[80-85] These methods can often be time consuming, reagent heavy, or require harsh additives to buffers. Geiger *et al.* further explored broadening in μFFE devices by investigating the effect of surface adsorption on the spatial and temporal dimensions of a 2D separation in a glass μFFE device.[79] They demonstrated that a significant amount of surface adsorption did not affect the spatial dimension broadening. This was as expected due to the nature of the separation. Analytes travel along the same trajectory throughout the channel based on the applied electric field, so there is no lateral movement from its trajectory once the analyte enters the channel. Surface adsorption did however, have a large effect on temporal broadening. If an analyte adsorbs to the surface in μFFE, and does not desorb quickly, the band broadens as the rest of the sample is pressure driven through the channel. In the case of proteins, surface adsorption caused analyte peaks to never return back to baseline without the need for extensive cleaning of the μFFE device.[79] This was attributed to the glass surface interacting strongly with the charged analytes and the proteins not dissociating from the surface.

1.3 Scope of the Thesis

Microfluidics devices are proving to be ideal for many applications. Their reduced reagent volumes, analysis time, and potential for increased sensitivity have resulted in the miniaturization of many separation techniques. Unfortunately, old microfluidic fabrication processes slow down the creative process. These processes can take months to get from idea to a functional device. Even recently developed fabrication techniques have significant drawbacks associated with them. Specifically, most still have a need for a master, or lack the ability to produce sufficiently small features. Chapter 2 will describe the development of a novel 3D printed μFFE device. The 3D printer that was used was tested, and shown to be able to produce reliable, small z feature sizes. The 3D printer was then used to produce a feature side and a fluidic access side of a μFFE device. These methods produced a fully functional μFFE device which was shown to be able to separate dyes and proteins. Chapter 3 will focus on the surface properties of the newly fabricated device. Surface adsorption in glass devices has been shown to be detrimental to 2D separations. It is necessary to assess the surface properties for the μFFE device to be used in 2D couplings successfully. In this chapter an nLC × μFFE coupling was achieved through simple modifications of the 3D printed device. Experiments were then performed to determine the surface adsorption properties of 3 fluorescent dyes. Peptide and protein samples were also assessed for comparison to glass devices as they typically adsorb strongly to glass microfluidic devices. Chapter 4 will explore the potential for coupling of µFFE devices with mass spectrometry. Flow stability and protein deposition onto a PVDF hydrophobic membrane are explored in an open edge glass microfluidic device. A highly modified 3D printed device was then developed and the open edge deposition compared. A novel ionization method was also explored to ionize proteins for mass spectrometric analysis directly from a hydrophobic protein trapping membrane.

Development of the novel 3D printed fabrication method presented in this work has led to many improvements in µFFE devices. The reduced cost and fabrication time associated with 3D printing encourages design creativity. Many 2D couplings are also now feasible due to the ease of modifications associated with these fabrication methods. Furthermore, the use of ABS eliminated surface adsorption of cationic analytes, making protein separations easier to perform. These achievements lead the way for highly customizable µFFE devices for a number of applications including previously difficult protein samples and mass spectrometry coupling.

Chapter 2

3D Printed Micro Free-Flow Electrophoresis Device

Anciaux, S. K.; Geiger, M.; Bowser, M. T. Analytical Chemistry 2016, 88, 7675-7682.

2.1 Summary

The cost, time, and restrictions on creative flexibility associated with current fabrication methods present significant challenges in the development and application of microfluidic devices. Additive manufacturing, also referred to as 3D printing, provides many advantages over existing methods. Utilizing 3D printing, devices can be made in a cost effective manner with the ability to rapidly prototype new designs. We have fabricated a µFFE device using a low cost, consumer grade 3D printer. Test prints were performed to determine the minimum feature sizes that could be reproducibly produced using 3D printing fabrication. Microfluidic ridges could be fabricated with dimensions as small as 20 µm high × 640 µm wide. Minimum valley dimensions were 30 µm wide × 130 µm wide. An acetone vapor bath was used to smooth ABS surfaces and facilitate bonding of fully enclosed channels. The surfaces of the 3D printed features were profiled and compared to a similar device fabricated in a glass substrate. Stable stream profiles were obtained in a 3D printed µFFE device. Separations of fluorescent dyes in the 3D printed device and its glass counterpart were comparable. A µFFE separation of myoglobin and cytochrome C was also demonstrated on a 3D printed device. Limits of detection for rhodamine 110 were determined to be 2 nM and 0.3 nM for the 3D printed and glass devices, respectively.

2.2 Introduction

Separations continue to be a major application of microfluidic devices including on-chip CE,[86] FFE[40,87] gel electrophoresis[88], LC,[89] and IEF.[87] Further development of these applications would benefit from the rapid prototyping, minimal cost, and reduced manufacturing time that 3D printing fabrication could provide. Unfortunately, very few microfluidic separations on 3D printed devices have been reported to date. Recently, the separation of three dyes was demonstrated on a fully 3D printed device.[90]

Recent advances in fabrication technologies have made production of μFFE devices faster and cheaper. As mentioned in Chapter 1, devices have been made faster by using liquid phase lithography, injection molding, photo curable polymers, multi-step lamination processes, among other processes. These fabrication methods all resulted in functional devices in less time than a typical glass device. Use of these methods did however often require expensive and specific machinery or the use of a master that is not attainable to many people.

FDM is the most easily accessible 3D printing technology available at this time.[68-76] Inexpensive, direct to consumer FDM printers are readily available. FDM is also compatible with inexpensive, widely available thermoplastic substrates. Unfortunately, FDM exhibits a number of drawbacks that have limited its application in microfluidics.[68-76] Deposition is limited by the nozzle dimensions, typically limiting resolution in the XY plane to ≥500 μm. Gaps between subsequent deposition passes give rise to porous finished products that are unable to contain pressurized fluids. Non-uniform deposition also produces opaque materials that makes on device optical detection challenging. These challenges have limited FDM printing to relatively large fluidics structures such as mixing channels and cell incubation chambers.[68-76] To the best of our knowledge, no electrophoretic separation has been reported to date in a microfluidic channel (i.e. ≤100 μm) produced by FDM printing.

In the current manuscript we assess the feasibility of FDM printing as a rapid prototyping strategy for producing low cost μFFE devices. While many alternative low cost fabrication strategies have been demonstrated for producing μFFE devices[25,54-58], many of these require specialized equipment or detailed fabrication steps. As stated by many other authors, the simplicity, availability and uniformity of 3D printing strategies suggest that this fabrication strategy will soon replace most current approaches for producing polymeric microfluidic devices in research labs.[68-76] To achieve this goal FDM printing must be able to produce devices with smaller channels with the structural integrity to withstand fluidic pressure in optically clear finished materials.

2.3 Experimental

2.3.1 Chemicals

All solutions were made with deionized water (18.3 MΩ; Millipore, Bedford, MA) and filtered with a 0.22 μm nitrocellulose membrane filter (Fisher Scientific, Fairlawn, NJ). μFFE separation buffer contained 300 μM Triton X-100 and 25 mM HEPES all of which were purchased from Sigma-Aldrich (St. Louis, MO). The pH of the buffer was adjusted to 7.00. Stock solutions of rhodamine 123, rhodamine 110 chloride and fluorescein (Sigma-Aldrich) were prepared at varying concentrations, in separation buffer. Stock solutions of myoglobin (equine skeletal muscle, Sigma-Aldrich) and cytochrome c (bovine heart, Sigma-Aldrich) were prepared in 10 mM $NaHCO_3$ (Mallinckrodt, Paris, KY) in water at concentrations of 1.1 and 1.2 mg/mL, respectively. A 10 mg/ mL Chromeo P503 (Active Motif, Carlsbad, CA) solution in DMSO (Sigma-Aldrich) was prepared to label the proteins. To perform the labeling, 10 μL of the Chromeo P503 dye solution was added to 490 μL of each protein solution and vortexed for 10 min. The vials were allowed to incubate at room temperature for 24 h before any separations were performed. The labeled proteins were stored at 0 °C when not in use. Piranha solution (2:1 H_2SO_4/H_2O_2) (Ashland Chemical, Dublin, OH) was used to clean glass wafers and etch Ti. (CAUTION: Piranha solution reacts violently with organic materials; it must be handled with extreme care.) GE-6 (Acon Technologies, INC., Pittson, PA) was used to etch Au. Concentrated HF (49%) (Ashland Chemical) was used to etch glass wafers. Silver conductive epoxy (MG Chemicals, Surrey, BC Canada) was used to make electrical connections to the glass μFFE device. Crystalbond 509 (SPI Supplies, West Chester, PA) was used to glue the inlet capillary into the glass device. Clear ABS (RepRapper, Hong Kong, China) was used for all 3D prints. 250 μm diameter Pt wire (Sigma Aldrich) was used for electrodes in the 3D printed device. Acetone (Fisher Scientific) was used to produce acetone vapor for smoothing and bonding of 3D printed layers. Epoxy (Loctite, Westlake, OH) was used to hold Pt wires in place and seal the electrode access holes.

2.3.2 Glass μFFE Design and Fabrication

Figure 2.1A shows a fully fabricated glass μFFE device. Fabrication followed procedures similar to those previously reported.[10,28,91] An 85 μm capillary channel was etched into two 1.1 mm borofloat glass wafers (Precision Glass & Optics, Santa Ana, CA) using standard photolithography techniques. A second photolithography step was performed, etching 80 μm deep electrode channels. Finally a third photolithography step etched the remaining features to 40 μm, resulting in two mirror image wafers with 205 μm deep capillary channels (~410 μm wide), 160 μm deep electrode channels, and 40 μm deep × 1 cm wide × 2.5 cm long separation channels. A 150 nm layer of Ti followed by a 150 nm layer of Au were deposited using a Temescal electron beam evaporator. A final photolithography step was performed to remove unwanted Ti and Au, resulting in patterned electrodes on one wafer. Access holes (1 mm) were drilled into the second wafer, and a ~90 nm think layer of amorphous silicon (aSi) was deposited. The two mirror image

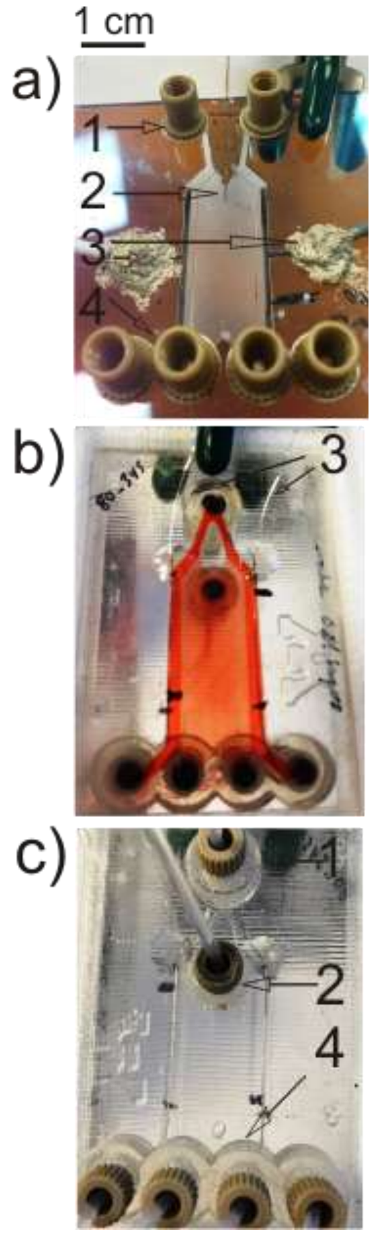

Figure 2.1. Images of a (A) glass μFFE device, (B) 3D printed μFFE device taken from the channel/detection side and (C) 3D printed μFFE device taken from the fluidic connection side. Labels highlight the (1) buffer inlets, (2) sample inlet, (3) electrode connections, and (4) outlets.

wafers were aligned and anodically bonded (900 V, 3 h, 450˚C, 5 μbar) using a Karl Suss SB-6 wafer bonder (Munich, Germany). Bonding the two mirror image wafers resulted in a 410 μm deep × 410 μm wide capillary channel, 320 μm deep electrode channels, and an 80 μm deep × 1 cm wide x 2.5 cm long separation channel. The bonded device was then diced at the University of Minnesota Electrical Engineering/Computer Science Machine Shop, exposing the capillary channel. Nanoports (Upchurch Scientific, Oak Harbor, WA) were aligned and affixed over the access holes using epoxy rings. Silver conductive epoxy was used to connect lead wires to the patterned electrodes. The device was then heated on a hot plate to ~150 ˚C while under vacuum. A 75 μm i.d. × 360 μm o.d fused silica capillary (Polymicro Tehcnologies, Phoeniz, AZ) was inserted into the capillary channel and bonded into place by pulling Crystalbond 509 through the remaining space between the capillary and the channel. The μFFE device was then perfused with 1 M NaOH solution to remove aSi from the channels.

2.3.3 3D Printed μFFE Design and Fabrication

Figures 2.1B and 2.1C show a fully fabricated μFFE device 3D printed using clear ABS plastic. Features of the top and bottom layers of the device were designed using AutoDesk Inventor (see Figure 2.2A). The CAD included 345 μM deep electrode channels and an 80 μm deep × 2.5 cm long × 1 cm wide separation channel. The design integrated threaded fluidic connection ports for the sample inlet, buffer inlet and waste outlets on the access side of the device. These were designed to be compatible with commercially available fittings (10-32 and 6-32 coned finger tight ferrules, IDEX, Science, Oak Harbor, WA). The sample inlet and electrode access holes were drilled using a 25 µm bit and drill press (Micro-Mark, Berkeley Heights, NJ). Several design modifications were made compared to the glass device including: moving the electrode access holes, rounding the sharp triangle feature at the buffer inlet, and widening the buffer outlet channels. The CAD file was then saved as a .STL file and uploaded to Cura (Version 14.12.1) (Ultimaker, Denmark). Both the feature side of the device, and the fluidic access side of the device were printed using an Ultimaker[2] (Ultimaker, Denmark) using the following parameters: 20-40 µm layer height, 10 mm/s printing speed, ~104% material flow rate, 85 ˚C bed temperature, and 260 ˚C nozzle temperature. The build plate was covered in Kapton® tape to improve adhesion of the ABS filament. After printing was completed (~14 hours) the feature and

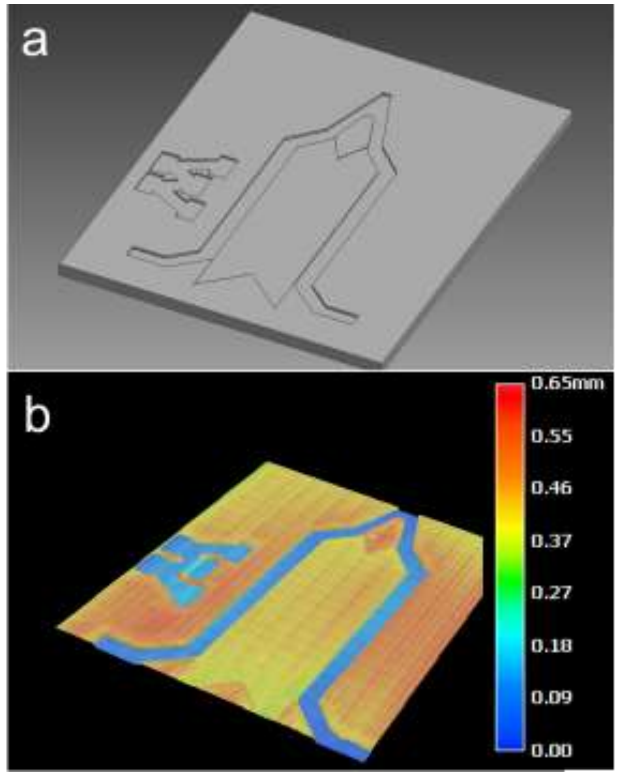

Figure 2.2. (a) Autodesk Inventor Professional CAD of the 3D printed µFFE device. Features were drawn with an 80 µm deep × 2.5 cm long × 1 cm wide separation channel and 345 µm deep × 2 mm wide electrode channels. (b) 3D stitched image of the channel layer of a 3D printed µFFE device recorded using a Keyence light microscope.

fluidic connection layers were bonded using an acetone vapor bath. To do this, two 5 cm long × 250 μm diameter platinum wires, were inserted into the access holes in the electrode channels on the feature side of the device. Acetone vapor was produced by heating the solvent in a Pyrex beaker on a hotplate set to 90 ºC (see Figure 2.3). Acetone is flammable and caution should be taken when heating. All acetone vapor bonding was performed in a fume hood and carefully monitored throughout the procedure. The feature side of the device was inserted into the acetone vapor with the features facing down. The features were exposed for ~1.5 min, removed and allowed to dry for 2-3 min. Similarly, the fluidic access layer was immersed in the acetone vapor flat side down for ~1.5 min and then allowed to dry ~1 min before bonding. Bonding was achieved by aligning the access holes over the device channels and lightly pressing the two layers together around the sides of the device. Epoxy was used to fix the Pt wires in place and seal the electrode access holes. The bonded device was allowed to dry overnight at ambient conditions. Electrode connections were made with lead wires and small

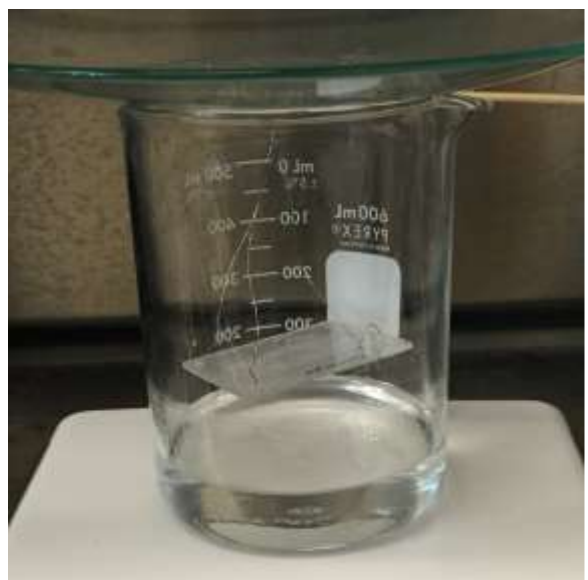

Figure 2.3. Image of the acetone vapor bath used to smooth and bond 3D printed ABS layers. The printed ABS layer is suspended above ~100 mL of heated acetone for 1.5 minutes.

copper alligator clips directly to the Pt wire in the device. The 3D printed device, when not in use, was stored with the channels filled with water and pumping at a low flow rate to prevent drying and as a consequence cracking of the ABS. The emergence of cracks greatly interfered with both flow and fluorescence detection. This storage method increases the useable lifetime of the device to several weeks instead of days.

2.3.4 μFFE Separations

Tefzel® Tubing (1/16” OD × 0.040”, IDEX Health and Science, Oak Harbor, WA) was connected directly to the printed access ports on the ABS μFFE device using modified commercially available fittings (10-32 and 6-32 coned finger tight ferrules, IDEX, Science, Oak Harbor,WA) and o-rings. Separation buffer and sample (500 nM fluorescein, 50 nM rhodamine 110, and 500 nM rhodamine 123) were pumped into the device using syringe pumps at 1.0 mL/min and 1 μL/min, respectively (Separation buffer pump: Model # 55-2222, Harvard Apparatus, Holliston, MA; Sample pump: New Era Pump Systems, Model # NE-300, Farmingdale, NY). During μFFE separations, the right electrode was grounded and a +50 V separation potential was applied to the left electrode using a power supply (PS310, Stanford Research Systems INC, Sunnyvale, CA). Separation buffer was pumped at 0.5 mL/min for protein separations and +70 V applied.

2.3.5 μFFE Detection and Data Collection

An AZ 100 stereomicroscope (Nikon Corp., Tokyo, Japan) mounted with a 100 W X-Cite fiber-optic metal halide lamp (Nikon Corp.) and Cascade

512B CCD camera (Photometrics, Tucson, AZ) was used for fluorescence imaging. Analyte detection was performed using 0.75× zoom to image the 1 cm wide separation channel 1.8 cm downstream from the sample inlet. For LIF detection, a 25 mW beam from a variable power 488 nm 150 mW diode pumped solid state laser (Sapphire, Coherent, Santa Clara, CA) was expanded to a ~2.5 cm wide by ~150 μm thick line across the μFFE separation channel directly below the microscope objective. The microscope was equipped with an Endow GFP emission filter cube (Nikon Corp) containing two bandpass filters (450-490 nm and 500-550 nm) and a dichroic mirror (495 nm cutoff). A 1.6× objective was used for collection with a 0.7× CCD camera lens. Images were acquired at a rate of 10 Hz and a gain of 3000. The entire setup was enclosed in a light tight enclosure (Newport, Irving, CA). Collected linescans of the separations were exported as a text file and background subtracted. The background signal was recorded at each pixel across the separation channel by averaging 3 linescans before sample introduction.

2.3.6 Depth Profiling

The surface depth profiles of 3D printed features were recorded using a VHX-5000 Keyence microscope (Itasca, IL). The 3D printed layers were set onto the ambient stage for imaging; black and glass backgrounds were used for layers imaged before or after the acetone vapor bath, respectively. Lighting and digital settings were optimized using the automatic “optimize” function. The imaging area was set in the X/Y plane across the device from outside the left electrode channel to the opposite electrode channel, perpendicularly through the separation channel (~1.5 cm). The depth was set to collect from the below the bottom of the electrode channels to above the top surface of the device in the Z dimension (~600 µm). The microscope moved the focal plane through each Z step (~10 µm) at 200× magnification, determining what portions of the image were in focus for each layer. The stage then moved, repeating the process across the entire imaging plane. Individual 3D images were then automatically stitched together, giving the full depth profile across the entire 3D printed layer.

2.4 Results and Discussion

2.4.1 Characterization of 3D Printer Resolution

The cost of consumer grade 3D printers has dropped dramatically while performance characteristics continue to improve. A variety of printers are currently available for several thousand dollars making the initial equipment outlay for entry into the field relatively modest. We performed initial experiments to characterize the minimum feature sizes that could be reliably printed using a low-cost, consumer grade, FDM printer. Minimum depth/height and width of valleys (i.e. structures dropped below the layer plane) and ridges (i.e. structures built above the layer plane) were assessed. Resolution in both the X/Y plane and Z (layer

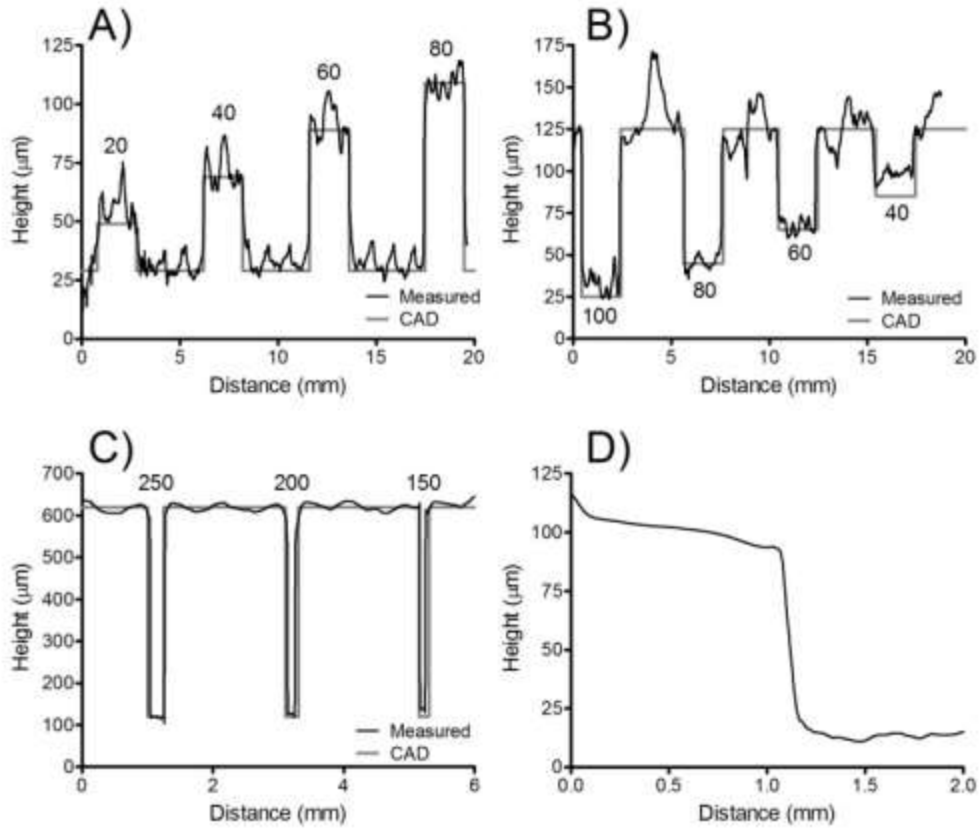

Figure 2.4. (A-C) Depth profiles of 3D printed features measured using a Keyence light microscope (black lines). Features were designed to assess the minimum (A) ridge height, (B) valley depth and (C) valley widths that could be produced. The layer depth of the 3D printer was set to 20 _m. Gray lines indicate the profile predicted by the CAD. Labels are the predicted feature size in µm. (D) Depth profile of the edge of an 80 µm deep channel etched into glass using HF.

depth) dimensions were compared. Printed structures were profiled using a Keyence microscope. The Keyence microscope is able to profile the topography of a device by determining the focal plane necessary to bring surface features into focus. For example, Figure 2.2B shows the topography of a 3D printed channel layer of a µFFE device, clearly showing different depths in the electrode channels, separation channel and the bonding surface. Figure 2.4 compares the topography measured using the Keyence microscope with the theoretical CAD profile for various 3D test

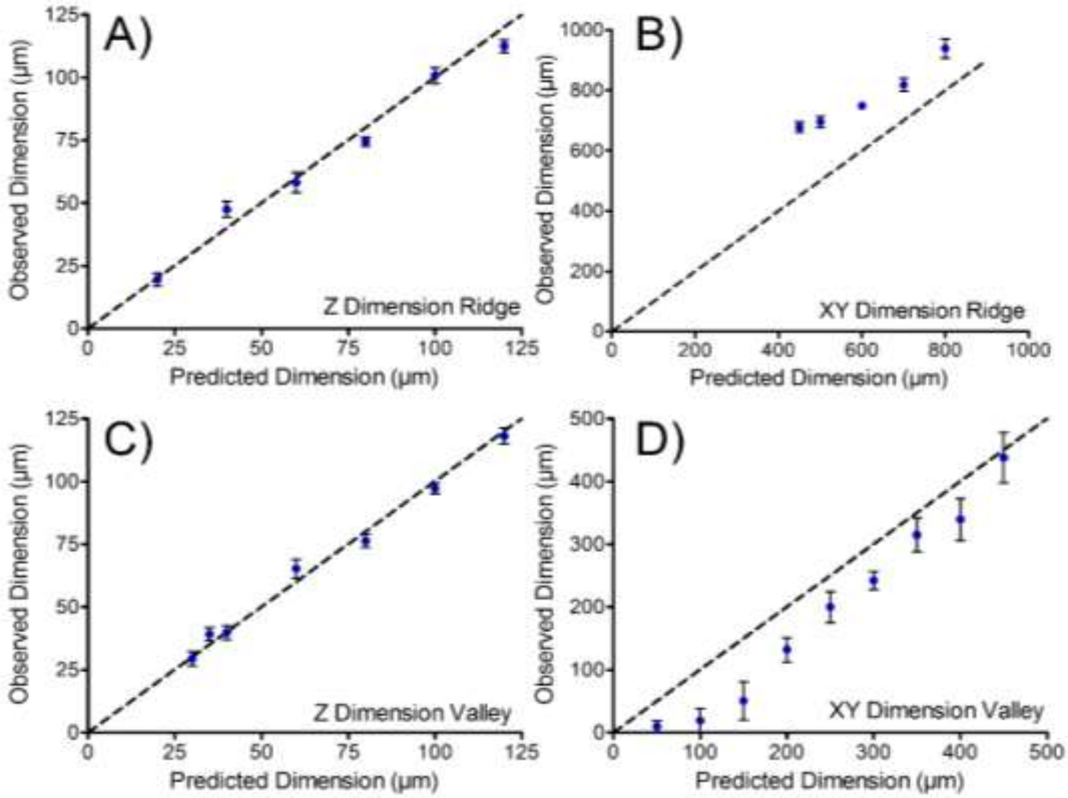

Figure 2.5. Comparison of feature sizes measured using a Keyence light microscope (observed) to those predicted by the CAD. 3D test prints were produced with features designed to assess the minimum (A) ridge height, (B) ridge width, (C) valley depth and (D) valley width that could be produced. The layer height of the 3D printer was set to 20 µm for all test prints. Dashed lines indicate ideal feature sizes predicted by the CAD file. Error bars indicate the standard error of n=4 measurements made on independently printed substrates.

prints. Figure 2.5 assesses this data quantitatively for n=4 independent test prints across a range of feature sizes. As shown in Figures 2.4A & 2.5A, ridges (i.e. structures printed above the layer plane) with heights as small as 20 µm could be produced reliably. This compares well with the 20 µm layer thickness entered into the printing parameters and suggests that these features were produced by a single pass of the FDM nozzle. Excellent linearity, accuracy and precision were observed for ridge heights ranging from 20 – 125 µm.

The minimum layer thickness of the printer is 20 µm, preventing ridges with smaller heights from being produced. The minimum width (XY dimension) of the ridges was limited by the 450 µm diameter of the extrusion nozzle. As shown in Figure 2.5B, over extrusion and feature deformation prior to cooling gives rise to ridges with larger widths than predicted in the CAD. This over extrusion limited the minimum width of ridges that could be fabricated to >680 µm. As shown in Figures 2.4B & 2.5C, valleys (i.e. structures that drop below the surface plane) with depths as small as 30 µm could be reliably produced. Excellent linearity, accuracy and precision were observed for valley depths over a range of 30 – 125 µm. Again, the fixed minimum layer depth of the printer prevented valleys with depths smaller than 30 µm from being be produced. As shown in Figures 2.4C & 2.5D, over extrusion was also observed in the XY dimensions of printed valleys, giving rise to narrower features than predicted by the CAD. Valleys with widths as low as 130 µm could be reliably produced, although at widths significantly lower than predicted in the CAD and with more variability than the other features assessed (see error ranges in Figure 2.5D). This suggests that experimental calibration for this dimension will be necessary, which would allow the effects of over extrusion in the XY plane to be accounted for in the CAD. The production of narrow valleys demonstrates that although the nozzle size limits the narrowest line of polymer that can be laid down on a single printing pass, subsequent passes of the printer head can be programmed to print adjacent surface features closer together than the dimensions of the extrusion nozzle, making the production of narrow valleys possible. This is an important distinction, since many microfluidic devices require fabrication of layers with narrow valley structures that can bonded together to produce enclosed channels rather than narrow features that extend above the surface plane. FDM was able to produce narrow valleys with high aspect ratios. The average slope (i.e. height/width) of the valley edges shown in Figure 2C was 73. For comparison, the isotropic etching used in glass fabrication gave rise to slope of 0.89 for the edge shown in Figure 2.4D. The

Table 2.1. Comparison between the observed minimum feature sizes and the predicted CAD dimensions for various 3D printed structures. Error limits are the standard error of n=4 measurements made on independently printed test features.

Dimension	**Feature**	**Figure**	**CAD (µm)**	**Actual (µm)**
Z	Ridge	Fig 2A	20	20 ± 3
X/Y	Ridge	--	450	680 ± 20
Z	Valley	Fig 2B	30	29 ± 3
X/Y	Valley	Fig 2C	200	130 ± 20

minimum feature sizes that could be produced in the XY plane and Z dimensions are summarized in Table 2.1.

The ~10 µm, regularly spaced, surface artifacts (i.e. peaks) observed in Figure 2.4 are a consequence of the FDM process. The FDM printer extrudes polymer in lines as the nozzle tracks back and forth across the structure. The extruded polymer solidifies before a perfectly smooth surface is produced. Setting the extrusion temperature to a point where the polymer flows freely when it hits the surface results in a loss of feature resolution. All profiles shown in Figure 2.4 were taken perpendicularly to the direction of the track artifacts to clearly show their contribution to the surface roughness of the printed layers.

Figure 2.6A shows the depth profile of the feature side of a 3D printed µFFE device. The depths of the separation and electrode channels (80 µm and 345 µm, respectively) match well with those predicted by the CAD. The aspect ratios of the channel boundaries are also very high. Significant surface roughness is observed in the separation and electrode channels due to the FDM tracking artifacts. Figure 2.7A shows an expanded profile of one of the electrode channels, clearly demonstrating the tracking artifacts.

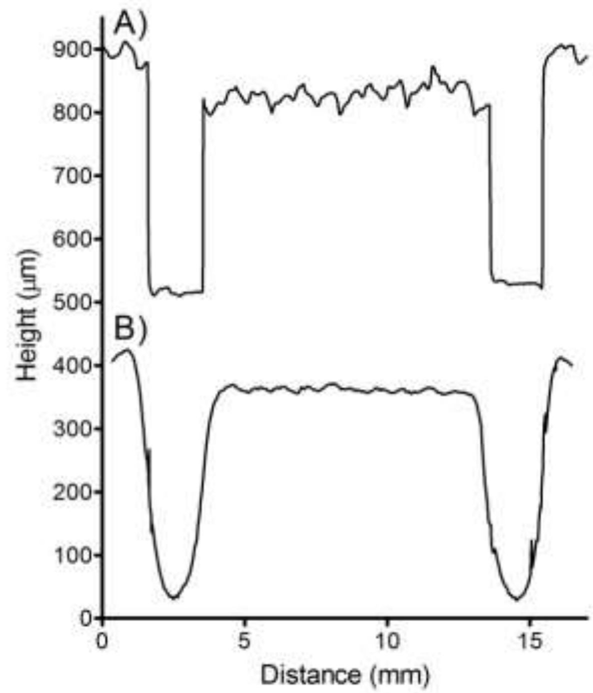

Figure 2.6. Depth profile of the channel layer of a 3D printed µFFE device (A) before and (B) after a 1.5 min acetone vapor bath. The dimensions predicted by the CAD are: 345 µm deep × 2 mm wide electrode channels and an 80 µm deep × 1 cm wide × 2.5 cm long separation channel. The layer depth of the 3D printer was set to 20 µm.

2.4.2 Acetone Vapor Bath

Solvent bonding provides a simple method for fusing two polymer layers.[67] The substrate is exposed to a solvent which partially dissolves a superficial polymer layer. When two layers are pressed together the partially dissolved polymers entangle, creating a strong bond when dried. Careful control of the solvent exposure is necessary to balance effective bonding with loss of feature resolution due to dissolution or softening of the polymer surface. We have chosen to apply acetone in a vapor bath due to the homogeneous application and enhanced control that this procedure affords. Figure 2.7 shows the effect of acetone exposure on the electrode channel features. Sharp features and a high aspect ratio are observed prior to acetone exposure (see Figure 2.7A). Exposure to the acetone vapor partially dissolves the surface layer smoothing the features. The rectangular channel becomes more rounded within 1-5 minutes of acetone exposure. Features with higher surface area dissolve more easily and are preferentially smoothed. As a result, acetone exposure effectively smooths the surface, eliminating the FDM tracking artifacts within 1 minute of exposure. Figure 2.6B shows the full profile of the feature side of the µFFE device after 1.5

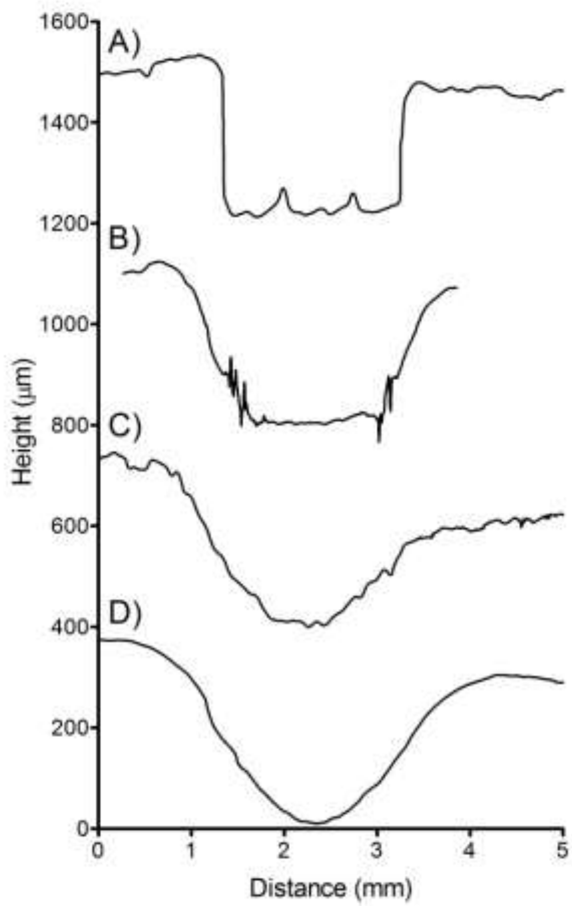

Figure 2.7. Depth profile of an electrode channel in a 3D printed µFFE device after exposure to an acetone vapor bath for (A) 0 min (B) 1 min, (C) 1.5 min and (D) >5 min.

minutes of acetone exposure. The depths of the channels remain largely unaffected while the surface smoothness in the separation channel is increased significantly. Prior to acetone vapor exposure, the surface height of the separation channel varied by ±14.5 μm (standard deviation). Acetone vapor exposure reduced this variation significantly to ±3.7 μm (standard deviation). Figure 2.8 compares optical images of the feature side of the μFFE device before and after acetone exposure. The acetone exposure removes the FDM tracking artifacts, improving surface smoothness and optical clarity. It should be noted that acetone exposure did not induce any noticeable clouding or discoloration of the ABS. Unlike liquid solvent bonding methods, vapor exposure leaves no marks associated with using a brush or applicator.

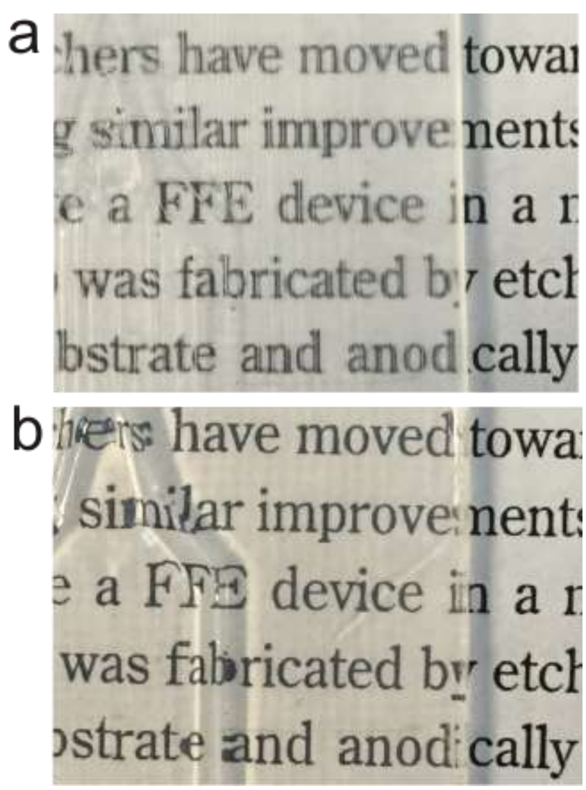

Figure 2.8. Optical image of the channel layer of a 3D printed μFFE device (A) before and (B) after 1.5 min. exposure to an acetone vapor bath.

A fully fabricated 3D printed μFFE device is shown in Figure 2.1C. Bonding the feature and access layers was achieved in <5 min. The heated acetone vapor bath simultaneously smoothed FDM tracking artifacts, bonded, and clarified the 3D printed device. The optimal acetone vapor exposure time to clarify the device, reduce ridges, and achieve a solid bond while minimizing loss of features was found to be

~1.5 minutes. Further exposure did not improve clarity or bonding effectiveness while feature definition continued to deteriorate. The optimum exposure time was also found to depend on the humidity and lab conditions. The precise exposure time was determined visually based on the appearance of the plastic. Bonding was most likely to be successful when the surface appeared smooth/glossy and could be easily indented. As shown in Figure 2.1B, solvent bonding effectively sealed the device and no leaks were observed when buffer was pumped through the separation channel.

2.4.3 µFFE Separation and Limits of Detection

Figure 2.9 shows a µFFE separation of three fluorescent dyes in a 3D printed device. Stable streams with linear trajectories were observed suggesting that 3D fabrication was able to produce a separation chamber with a well-defined geometry and no major defects that would affect buffer flow or electric field. Figure 2.10 presents linescans of the same separation recorded using LIF detection.

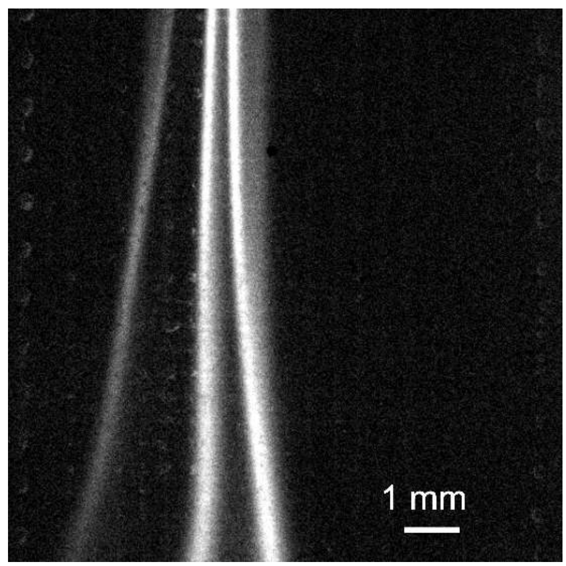

Figure 2.9. A stream profile of (left to right) fluorescein (1.56 µM), rhodamine 110 (1.37 µM), and rhodamine 123 (26.3 µM) flowing through a 3D printed µFFE device. +150 V was applied to the left electrode while the right was held at ground.

Increasing the electric field pulled the streams apart improving resolution similar to previous reports in an all glass µFFE device.[10,28] Baseline resolution was obtained at potentials >50V. Several of the peaks appear to exhibit artifacts or splitting. As shown in Figure 2.9, well defined streams are observed in the separation channel suggesting that flow irregularities or instability are not the cause of the artifacts. Instead fabrication defects give rise to detection deadspots where recorded fluorescence is lower than expected. It is hypothesized that the small ridges remaining after the acetone vapor bath either change the path length in the channel or redirect the light away from the camera. We are continuing to refine the FDM fabrication protocol to minimize the occurrence of these defects.

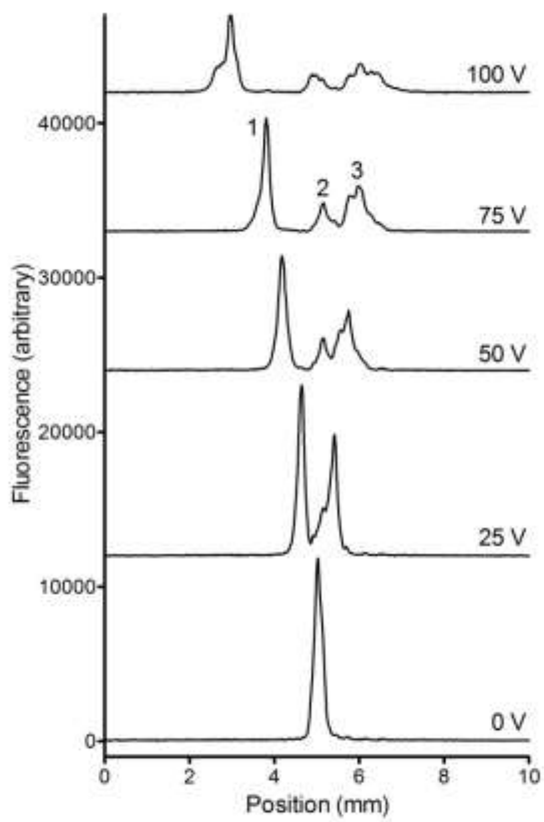

Figure 2.10. LIF linescans of µFFE separations of (1) fluorescein (500 nM), (2) rhodamine 110 (50 nM), and (3) rhodamine 123 (500nM) performed in a 3D printed device. +0 – 100 V was applied at the left electrode

Figure 2.11 shows a µFFE separation of Chromeo P503 labeled myoglobin and cytochrome C performed in a 3D printed device. These proteins are difficult to separate in capillary electrophoresis (CE) or microfluidic devices due to their strong adsorption to glass surfaces.[79] No surface coatings, ion pairing agents or other buffer additives were necessary to achieve resolution suggesting that ABS may provide a native surface that minimizes protein adsorption. Near baseline resolution is achieved in the 3D printed µFFE device. The peaks for myoglobin and cytochrome c are broader and less symmetric than those observe for fluorescein, rhodamine 110 and rhodamine 123. This broadening is consistent with µFFE separations performed in glass devices and is thought to be a result of heterogeneity in the proteins themselves due to multiple labeling sites, posttranslational modifications or tertiary structure.[79]

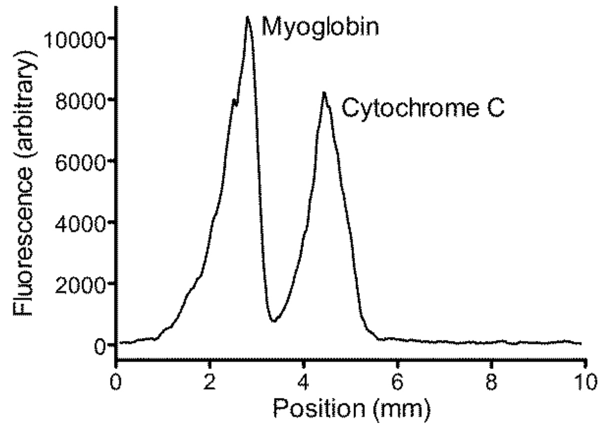

Figure 2.11. µFFE separation of Chromeo P503 labeled myoglobin (0.04 mg/mL) and cytochrome C (0.9 mg/mL) performed in a 3D printed device.

2.4.4 Comparison of 3D Printed and Glass µFFE Devices.

Figure 2.12 directly compares a µFFE separation recorded on a 3D printed device with one performed using a similar device fabricated in glass. The sample and all operating parameters (i.e. voltage, flow rates, etc.) were identical. The only design difference between the two devices was

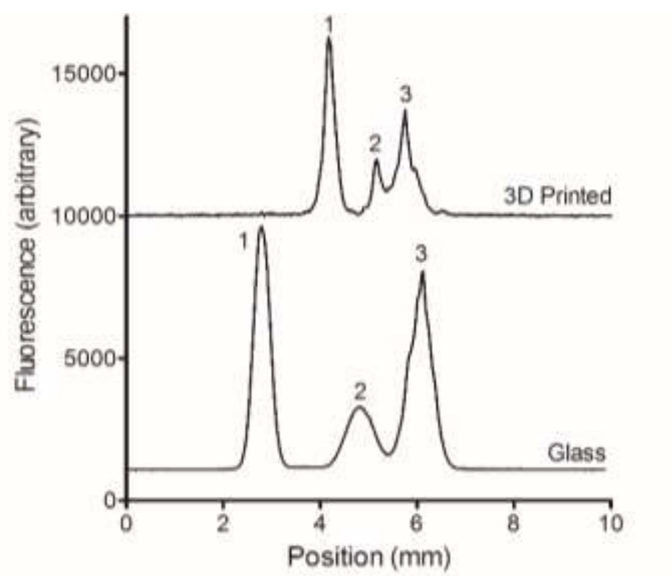

Figure 2.12. Comparison of µFFE separations performed in a 3D printed device (top) and one fabricated in glass (bottom). Analytes are (1) fluorescein (500 nM), (2) rhodamine 110 (50 nM), and (3) rhodamine 123 (500nM). +50 V was applied to the left electrode. Linescans were obtained using LIF detection.

the size of the electrode channels, which were increased in the 3D printed device to match the volume lost due to the Pt wire electrodes. The separation is qualitatively similar in both devices. The observed difference in separation power[91] (i.e. peak spreading) may be due to subtle variations in the final device dimensions, which could give rise to significant differences in buffer linear velocity or electric field in the separation channel. The electroosmotic flow (EOF) recorded in the 3D printed μFFE was ~27-fold lower than that observed in the glass device (1.4×10^{-7} $cm^2V^{-1}s^{-1}$ *vs.* 3.8×10^{-6} $cm^2V^{-1}s^{-1}$). EOF was expected to be suppressed in the 3D printed device since the ABS polymer used for fabrication is neutral.

As shown in Figure 2.8, 3D printing followed by an acetone vapor bath produced an optically clear device. Only 14% of signal intensity is lost when compared to the glass device (see Figure 2.12). The background noise was ~5-fold larger in the 3D printed μFFE than the glass device. Small surface defects remained even after the acetone vapor bath which gave rise to increased scattering in the separation channel. The limits of detection (LOD) recorded for fluorescein, rhodamine 110, and rhodamine 123 in the 3D printed μFFE device were 5 nM, 2 nM and 10 nM, respectively. These LOD's were ~10-fold worse than those recorded in the glass device (i.e. 0.6 nM, 0.3 nM, and 3 nM for fluorescein, rhodamine 110, and rhodamine 123, respectively). This decrease in LOD is typical when polymeric devices are compared to those fabricated in glass. Higher scatter and background fluorescence are common in polymeric substrates, increasing the observed noise.[92,93]

2.5 Conclusions

We assessed a bench top, low cost, consumer grade, FDM 3D printer for its potential to fabricate microfluidic devices. Features were produced with 130 μm resolution in the X/Y plane and 20 μm resolution in the Z axis (i.e. prior to exposure to the acetone vapor bath). A 3D printed μFFE device was fabricated. ABS layers containing the fluidic channels were designed and printed. Fluid access holes and connection ports compatible with commercial fittings were integrated directly into the device. Fabrication was facilitated by an acetone vapor bath that simultaneously accomplished bonding, electrode incorporation, clarification, and smoothing in less than 5 minutes. The performance of the μFFE device was assessed using a separation of three fluorescent dyes. Observed separations were similar to those recorded in a glass μFFE device. LOD's measured on the 3D printed μFFE device ranged from 2-10 nM, ~10-fold worse than those observed on a similar glass device.

A fully functional, 3D printed μFFE device was fabricated for ~$0.20 in material costs in <36 hours. Less than 10 min of the overall fabrication compared to >$2000 and weeks of labor to produce a similar glass device. time involved direct manual intervention (i.e. bonding and electrode insertion). FDM parameters were set to maximize resolution and space filling resulting in relatively long print times (~14 hours). Similarly, the device was allowed dry overnight after bonding to ensure a robust seal. The reduced cost and fabrication time associated with 3D printing encourages design creativity. Rapid prototyping is easily incorporated into the design cycle since making modifications is as simple as changing the CAD file and printing a new device. CAD files are easily transferred allowing new designs to be quickly adopted by colleagues worldwide, further enhancing innovation in the field.

Chapter 3

Minimal Surface Adsorption is Observed in 3D Printed Acrylonitrile Butadiene Styrene Micro Free-Flow Electrophoresis Devices

3.1 Summary

As shown in Chapter 2, the ability to fully fabricate a device by FDM in less than 2 days was achieved. This leads to the ability to make quick modification of microfluidic devices. Furthermore, during the protein separation in Chapter 2, it was noted that the device did not need cleaned after the protein separation, unlike the necessary step of flushing out adsorbed proteins from a glass device. Due to this the investigation of the surface properties and adsorption tendencies to ABS was investigated, as it was hypothesized that there would minimal surface adsorption in the device, which would be a huge advantage for 2D separations.

Adsorption of analytes to surfaces presents significant challenges in many separations. Surface adsorption often becomes a significant source of peak broadening and asymmetry. To reduce surface adsorption, coatings and harsh buffer additives are often needed. The ability to perform a separation without the need of these conditions would be highly desirable. 3D printing presents a method for cost effective production of microfluidic devices. The decrease in time associated with using 3D printing also allows for rapid prototyping of new designs in a variety of polymers with different surface characteristics. We have 3D printed and fabricated a µFFE device in ABS that exhibits minimal surface adsorption with the use of no coatings or buffer additives. This result was confirmed using nano-liquid chromatography (nLC) x µFFE separations of rhodamine 110, rhodamine 123, and fluorescein. Peak widths and asymmetries were measured in both temporal and spatial dimensions. No significant broadening was seen in the spatial or temporal dimension for the fluorescent dyes. Chromeo P503 labeled myoglobin and cytochrome c were also assessed, and minimal surface adsorption was observed in both dimensions. A separation of a tryptic bovine serum albumin (BSA) digest was performed and also demonstrated the lack of adsorption in the ABS device.

3.2 Introduction

We have previously demonstrated a µFFE device was fabricated by FDM in ABS using an acetone vapor bath bonding method. [94] The 3D printed polymeric device was made in less than two days and separations of fluorescent dyes and proteins demonstrated. The ability to manufacture devices so quickly allows for prototyping of new devices much faster than previous methods, but little is known about the surface properties of 3D printed microfluidic devices.

The use of thermoplastics in 3D printing allows for the selection of the µFFE device substrate. In the current work, only ABS is explored. The interactions of the different types of thermoplastics with analytes of interest can play a large role in the quality of the separation. If an analyte interacts strongly with the surface, broadening can occur. In glass µFFE devices Geiger and Bowser experimentally showed that surface adsorption does not affect band broadening in the spatial dimension of µFFE. Surface adsorption did affect the widths of peaks in the time dimension.[79] In their experiments temporal peak widths for positively charged analytes increased as much as 10 fold for small molecule analytes. Proteins adsorbed nearly irreversibly and required extensive flushing and cleaning of the device. They noted that only the temporal dimension was affected by this surface adsorption. Even extensive surface adsorption had no effect on peak width or position in the µFFE spatial dimension. This is attributed to the nature of the µFFE separation. As the analyte enters the separation channel, it stays on the same trajectory to the outlet throughout the separation. Even if there is surface adsorption there is no movement laterally other than that attributed to the broadening described in the second and third term of Equation 1.1. In this experiment the separation was made more difficult in that it required PEO coating of the µFFE device and addition of 8 M urea to the µFFE separation buffer in order to reduce surface adsorption such that the separation could be succesful.[40] Broadening in these separation methods can be described by peak asymmetry and peak widths. Peak asymmetry is defined as the ratio of the width of the peak tail to the width of the peak front, taken at 1/10 of the peak height. Typically a peak with ratio greater than 2 is regarded as asymmetric with the peak width taken at half height.

The presence of surface adsorption can result in highly distorted peak shapes. Peak tailing is often seen as analytes adsorb to the channel surface, and then desorb over time. In separation techniques utilizing glass surfaces, interactions arise due to the ionization of the silica surfaces in CE at pH > 3[95] and stationary phases containing unevenly distributed silanol groups.[96-98] PDMS devices also exhibit non-specific protein adsorption on bare PDMS. This has been attributed to its hydrophobic nature. A number of studies have been performed to characterize the effect of surface adsorption, and methods developed to reduce the amount of interactions.[77,78,99,100] Common methods for overcoming this in CE include buffer modifications and the use of polymers to coat the capillary surface.[80-85] For nLC poor peak shape and lowered separation performance can be overcome with the addition of ion pairing agents.[101] For PDMS polymer surface modifications have been utilized to reduce adsorption in PDMS devices by increasing hydrophilicity of the surface.[102,103]

Not much is known about surface adsorption in 3D printed devices. Adsorption of molecules such as proteins and lipids to 3D printed materials has been hypothesized to reduce the detected signal due to adsorption seen in other applications with similar materials, but has not been experimentally proven.[104,105] 3D printed filament material composition is often proprietary, but many filaments are acrylate and ABS based. ABS has been described in the literature as having a contact angle of 72 degrees with water, which is slightly hydrophilic.[106] If surface adsorption is abundant in these 3D printed devices, they would not be ideal for 2D separations.

In the current manuscript we assess surface adsorption in an ABS 3D printed µFFE device. In glass devices, the spatial asymmetry has been shown to be unaffected by surface adsorption in µFFE, but the significant asymmetries and peak widths in the temporal dimension were observed as surface adsorption increases. While 2D separations have been done in µFFE, buffer additives and polymer coatings were necessary. Polymer coatings require many reagents, are time consuming, and need regenerated frequently.[40] The surface adsorption in the ABS 3D printed device is assessed for use in 2D separations without the use of buffer additives or channel coatings.

3.3 Experimental

3.3.1 Chemicals and Reagents

All solutions were prepared using deionized water (18.3 MΩ, Milli-Q; Millipore, Bedford, MA) and filtered through a 0.22 µm nitrocellulose membrane filter (Fisher Scientific, Fairlawn, NJ) unless otherwise stated. The µFFE separation buffer contained 10% MeOH and 25 mM HEPES (Sigma-Aldrich, St. Louis, MO), adjusted to pH = 7.00 using 1 M NaOH (Macron Chemicals, Center Valley, PA**).** Eluents for nLC were prepared using LC-MS grade methanol, acetonitrile, water (J.T. Baker, Phillipsburg, NJ) and trifluoroacetic acid (TFA, Sigma Aldrich). Stock solutions of rhodamine 110, rhodamine 123, and fluorescein (Sigma-Aldrich) were prepared in 190 proof ethanol (Fisher Scientific) at 0.8 mg/mL, 0.8 mg/mL, and 1.2 mg/mL respectively. Stock solutions were diluted in 0.1% TFA to final concentrations. Stock solutions of myoglobin (equine skeletal muscle, Sigma-Aldrich) and cytochrome c (bovine heart, Sigma-Aldrich) were prepared in 10 mM aqueous $NaHCO_3$ (Mallinckrodt, Paris, KY) at concentrations of 1.1 and 1.6 mg/mL, respectively. To label the proteins, a 10 mg/mL Chromeo P503 (Active Motif, Carlsbad, CA) solution in DMSO (Sigma-Aldrich) was prepared. 10 µL of the Chromeo P503 dye solution was added to 490 µL of each protein solution and vortexed for 10 min. The vials were incubated at room temperature for 24 h.

When not in use the proteins were stored at -4 °C. BSA (Sigma Aldrich) was digested with trypsin following a standard digestion procedure. 1.0 mg of BSA was dissolved in 1.00 mL of 25 mM $NaHCO_4$ with 6.0 M urea. A standard reduction was then performed using tris(2-carboxyethyl)phosphine, (TCEP, Pierce Chemical, Rockford, IL) at 37 ^oC for 1 h in the dark, and followed by alkylation with iodoacetamide (IAA, Sigma Aldrich) for 1 h at 37 ^oC in the dark. Sequencing grade trypsin (Promega, Madison, WI) was then used in a 1:30 w/w ratio to digest the BSA sample overnight at 37 ^oC. The newly digested sample was lyophilized under vacuum and stored at -80^oC until analysis. The BSA digest sample was thawed and dissolved in 1.0 mL of 10 mM $NaHCO_3$. To label the peptides, a 10 mg/mL Chromeo P503 solution in DMSO was prepared. 10 μL of the Chromeo P503 solution was added to 490 μL of peptide solution and vortexed for 10 min. The vials were incubated at room temperature for 24 h. Labeled samples were filtered through 0.45 cellulose acetate syringe filters (Sterlitech, Kent, WA). Clear ABS (RepRapper, Hong Kong, China) was used for all 3D prints. 250 μm diameter Pt wire (Sigma Aldrich) was used for electrodes. Acetone (Fisher Scientific) was used to produce acetone vapor for smoothing and bonding of 3D printed layers. Epoxy (Loctite, Westlake, OH) was used to affix Pt wires in place and seal the electrode access holes.

3.3.2 3D Printed μFFE Design and Fabrication

Figure 3.1 shows a 3D printed μFFE device with a capillary sample inlet printed using clear ABS filament. Features of the top and bottom layers of the device were designed using AutoDesk Inventor. The CAD included 345 μM deep electrode channels and an 80 μm deep × 2.5 cm long × 1 cm wide separation channel. The design integrated threaded fluidic connection ports for the sample inlet, buffer inlet and waste outlets on the access side of the device (Figure 3.2). These ports were designed to be compatible with commercially available fittings (10-32 and 6-32 coned finger tight ferrules, IDEX, Science, Oak Harbor, WA). The CAD file was saved as a .STL file and uploaded to Cura (Version 14.12.1) (Ultimaker, Denmark). The feature side and the fluidic access side of the device were printed using an Ultimaker^2 (Ultimaker, Denmark) using the following parameters: 40 μm layer height, 10 mm/s printing speed, ~104% material flow rate, 85 ˚C bed temperature, and 260 ˚C nozzle temperature. Kapton® tape was used to cover the build plate to improve adhesion of the ABS filament. Electrode access holes were drilled into the feature side of the device at a 45 degree angle using a drill press (Micro-Mark, Berkeley Heights, NJ) fitted with a 25 μm bit. Electrodes (5

Figure 3.1. 3D printed μFFE device with a capillary sample inlet. The device is filled with food dye to demonstrate that no leaking was observed after bonding and concurrent capillary and electrode placement.

cm long × 250 μm diameter platinum wires) were inserted through the access holes in the electrode channels on the feature side of the device before bonding. Acetone vapor was produced by heating the solvent in a Pyrex beaker on a hotplate set to 90 ºC.[107] Acetone is flammable and caution should be taken when heating. All acetone vapor bonding was performed in a fume hood and carefully monitored throughout the procedure. The feature side of the device was inserted into the acetone vapor with the features facing down. The features were exposed for ~1.5 min, removed and allowed to dry for 2-3 min. A 20 μm ID/280 μm OD capillary was aligned by hand on the feature side of the device immediately after it had been exposed to acetone vapor. Next, the fluidic access layer was immersed in the acetone vapor flat side down for ~1.5 min and then allowed to dry ~1 min before bonding. Bonding was achieved by aligning the access holes over the device channels and lightly pressing the two layers together around the sides of the device. Epoxy was used to fix the Pt wires in place and seal the electrode access holes. The bonded device was allowed to dry overnight at ambient conditions. Electrode connections were made with connecting wires and small copper alligator clips directly to the Pt wire in the device. The 3D printed device, when not in use, was stored with the channels filled with water pumped at 0.25 mL/h to prevent drying and as a

Figure 3.2. Image of the μFFE device showing the 1) buffer inlet ports, 2) capillary sample inlet, 3) electrode connections, and 4) buffer outlet ports. The device was 3D printed in ABS with an 80 μm separation channel 345 μm and electrode channels.

consequence cracking of the ABS. The device used in the current work has been functional for over 6 months.

3.3.3 Nano-Liquid Chromatography

A Thermo-Dionex UltiMate3000 RSLC nano pump with WPS autosampler (Sunnyvale, CA) was used for LC separations. The analytical column (Thermo-Dionex Part number 164562) was 75 µm i.d. × 15 cm long packed with 2 µm Acclaim PepMap C18 particles. For the fluorescent dye separations mobile phase A was 100% H_2O and mobile phase B was 90:10 MeOH:H_2O. An isocratic composition of 85:15 B:A was chosen, using 0.1 µL injection and a 300 nL/min flow rate. For protein adsorption and BSA tryptic peptide separation experiments mobile phase A was H_2O with 0.1% TFA and mobile phase B was 90:10 ACN:H_2O with 0.1% TFA. An isocratic composition of 60:40 B:A was chosen for the protein separation, using 0.25 µL injection and a 300 nL/min flow rate**.** For the BSA tryptic peptide separation a gradient from 30% to 95% B was applied in 10 min after holding at 10% B for 3 min. The injection volume was 1.0 µL, and the flow rate was 300 nL/min.

3.3.4 µFFE Separations

Separation buffer was pumped into the device using syringe pumps at 0.6 mL/min (Model # 55- 2222, Harvard Apparatus, Holliston, MA). The sample eluted off the nLC at 300 nL/min. During µFFE dye separations, the right electrode was grounded and a +60 V separation potential was applied to the left electrode using a power supply (PS310, Stanford Research Systems INC, Sunnyvale, CA). Tefzel® Tubing (1/16” OD × 0.040”, IDEX Health and Science, Oak Harbor, WA) was connected directly to the printed access ports on the ABS μFFE device using modified commercially available fittings (6-32 coned finger tight ferrules, IDEX, Science, Oak Harbor,WA) and o-rings.

3.3.5 μFFE Detection and Data Collection

An AZ 100 stereomicroscope (Nikon Corp., Tokyo, Japan) mounted with a 100 W X-Cite fiber-optic metal halide lamp (Nikon Corp.) and Cascade 512B CCD camera (Photometrics, Tucson, AZ) was used for fluorescence imaging. The microscope was equipped with an Endow GFP emission filter cube (Nikon Corp) containing two bandpass filters (450-490 nm and 500-550 nm) and a dichroic mirror (495 nm cutoff). A 1.6× objective was used for collection with a 0.7× CCD camera lens. Images were acquired at a rate of 10 Hz and a gain of 3000. For the Chromeo dye labeled proteins a custom filter cube was used (Nikon Corp) containing two bandpass filters (470−500 and 570−640 nm) and a dichroic mirror (500 nm cutoff). Analyte detection was performed using 0.75× zoom to image the 1 cm wide separation channel at various distances downstream from the sample inlet. For LIF detection, a 50 mW beam from a variable power 488 nm 150 mW diode pumped solid state laser (Sapphire, Coherent, Santa Clara, CA) was expanded to a ∼2.5 cm wide by ∼150 μm thick line across the μFEE separation channel directly below the microscope objective. For fluorescent dyes the line was positioned at various distances down the chip to measure broadening effects. For proteins the line was positioned 20.5 mm down the separation channel. The entire setup was enclosed in a light tight enclosure (Newport, Irving, CA). For all adsorption experiments, a separate piece of 20 μm i.d. × 280 μm capillary was connected to the capillary placed in the chip using a zero dead volume union (Upchurch Scientific). The total length from the column to the end of the capillary in the μFFE device was 85 cm. The nLC pump was controlled using Chromeleon v6.8 software (Thermo-Dionex). Once logged, all data was processed using in-house Matlab programs. Collected linescans of the μFFE separations were exported as a text file and background subtracted. Cutter v5.046 was used to process linescans and chromatograms. Asymmetry values were calculated by fitting peaks to a third degree Gaussian function using the CurvFit application in Matlab for the extracted linescans, and a sixth degree Guassian function for the extracted chromatograms. Peaks were assessed at 1/10 the max height to determine asymmetry.

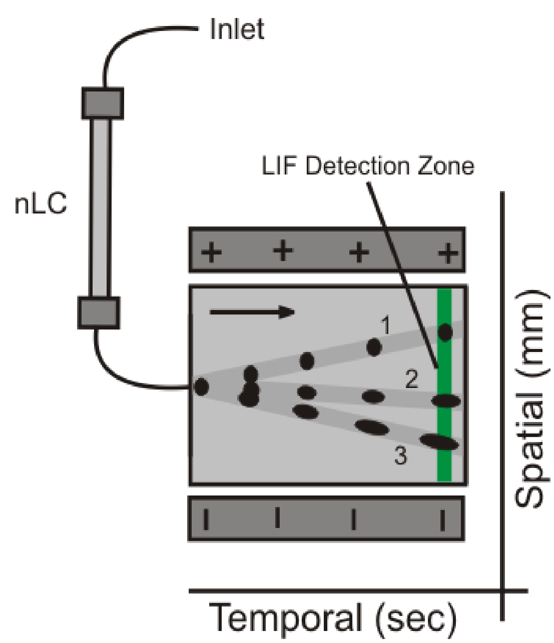

Figure 3.3. Diagram of nLC × μFFE instrumental setup. Analyte peaks flow directly into the μFFE separation channel as they elute off the nLC column and then separated laterally based on their electrophoretic mobility. Temporal broadening due to surface adsorption is depicted in the streams with 1) no surface adsorption, 2) moderate adsorption, and 3) high adsorption. Axes are drawn to show what dimensions are attributed to which type of broadening.

3.4 Results and Discussion

3.4.1 Interface Broadening

Geiger and Bowser have described a fabrication scheme for creating a zero dead volume nLC × μFEE interface. This was achieved by inserting a capillary into the separation channel through the side of the μFEE device (see Figure 1.5 and 3.3).[40] Dead volume at an interface can lead to sample mixing and increased broadening. Introduction of the sample through the side of the device, directly into the μFEE dimension greatly reduces dead volume and allows for retention of the achieved peak capacity.[40] In glass devices a deep channel was wet etched during fabrication and a capillary inserted after manufacturing the device and bonded in place. Utilizing 3D printing, the capillary is aligned by hand on the feature side of the device during the acetone vapor bonding step, adding only a few seconds to the method. This capillary introduction method has been shown to be easy to incorporate, and robust. A completed 3D printed device with capillary inlet is shown in figure Figure 3.2. The overlay in Figure 3.4 compares peak widths observed before and after the interface. The peak shapes observed before and after the interface are nearly identical, with minimal increase in peak width. Due to this, minimal broadening is attributed to the introduction of the capillary as the sample inlet for the 3D printed device.

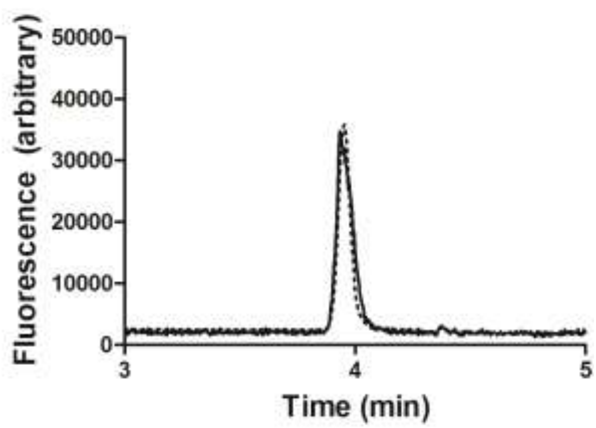

Figure 3.4. Overlay comparing peak shape of Rhodamine 110 prior to (dashed line) and immediately after (solid line) the nLC × μFFE interface. Chromatographs were aligned to emphasize comparisons in peak shape.

3.4.2 nLC $\times$ µFFE of Fluorescent Dyes

The nLC was used to introduce a discrete bolus of analyte into the µFEE separation to assess the effect of surface adsorption on the ABS – 3D printed device. Both spatial and temporal broadening were measured. Figure 3.5 shows 2D nLC $\times$ FFE separations of fluorescein and rhodamine 123 recorded at 2.0 mm, 10.0 mm, and 20.5 mm positions on the chip, relative to the capillary inlet. The first dimension is the time required to reach the detector (i.e. nLC retention time) and the second dimension is the position that the analyte crosses the detection zone (i.e. µFFE deflection distance). The intent was to inject a discrete bolus into the µFFE separation device, though some retention is seen in the 1st dimension. Due to the increased time in the electric field, resolution in the µFFE dimension increased as the analytes traveled further through the separation channel. Qualitatively there is minimal temporal broadening of the fluorescent dyes as they traverse the µFFE channel. In glass devices rhodamine 123 exhibits significant surface adsorption which gives rise to significant broadening in the temporal dimension as the peak travels through the µFFE separation channel.

3.4.3 Temporal Peak Widths

To investigate surface adsorption of analytes on the temporal dimension in the ABS device, chromatograms were recorded for each fluorescent dye at various distances along the µFFE separation channel. Chromatograms shown in Figure 3.6A are overlays of the three dyes as they traverse the separation channel. Visually, fluorescein and rhodamine 123 maintain their peak shape in both the spatial and temporal dimensions throughout the separation. Rhodamine 110 peak shape changes the most as it travels through the separation channel.

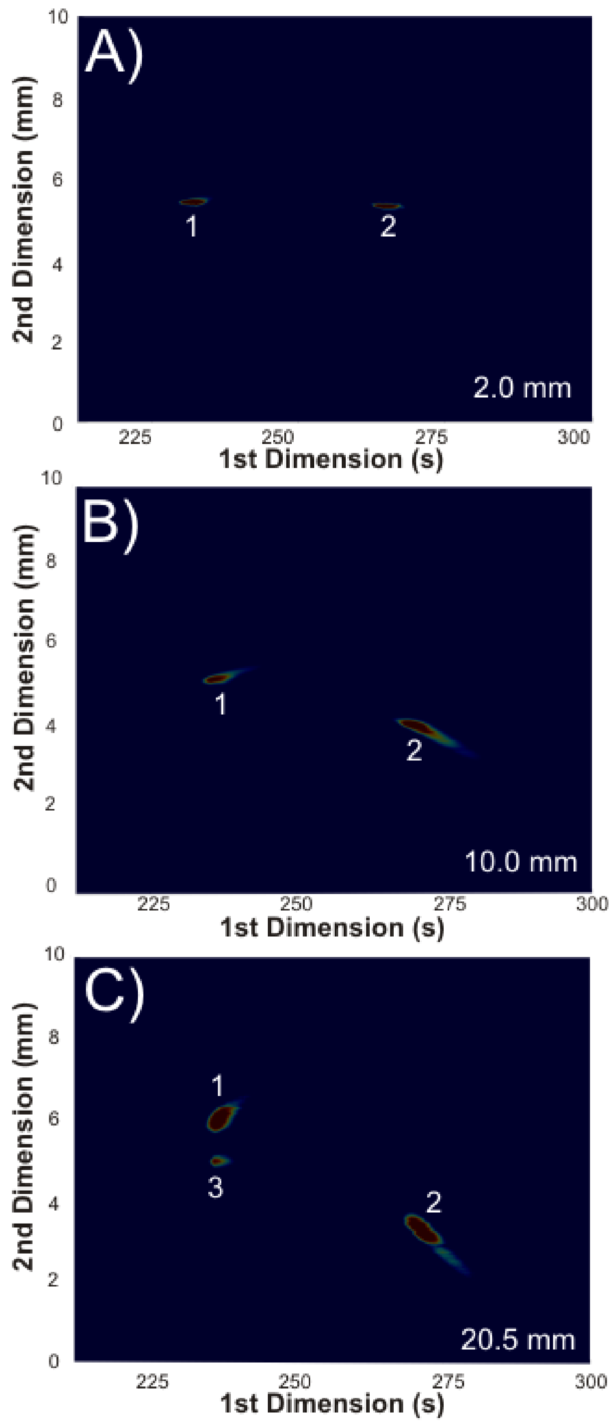

Figure 3.5. 2D nLC × µFFE separations of (1) rhodamine 123, (2) fluorescein, and (3) rhodamine 110 recorded measured in the µFFE separation channel (A) 2.0 mm, (B) 10.0 mm, and (C) 20.5 mm from the sample inlet. The first dimension is the nLC time and the second dimension is the µFFE deflection distance. Rhodamine 110 is absent from (A) and (B) because it could not be fully resolved from rhodamine 123. These samples were run separately.

To further explore adsorption in the device, peak widths were determined and evaluated. As shown in Figure 3.6B, the temporal peak width of rhodamine 110 trends upward but remains less than 10 seconds as the peak travels through the device. Rhodamine 123 and fluorescein have constant peak widths of ~5 s as they traverse the device. With previous glass devices, rhodamine 123 increased from a 10 s peak width at the capillary inlet, to a >50 s peak width at the outlet of the device.[79] That is a 5x increase in peak width for rhodamine 123 in an untreated glass device. A 2x increase was seen in peak width for rhodamine 110 in the ABS device. In glass devices, positively charged species were found to adsorb to the negatively charged glass surface.[79] For rhodamine 123, this large reduction in peak width from the glass device to the 3D printed ABS device is attributed to the decrease in strength of the surface interactions between the neutral ABS and the +1 charge Rhodamine 123. Rhodamine 110 exhibited some surface interaction which is attributed to its zwitterionic, net neutral, nature being more similar to the neutral ABS and exhibiting stronger interactions. Due to the lack of surface adsorption, no broadening was observed for both rhodamine 123 and fluorescein. For rhodamine 110, only modest broadening was observed.

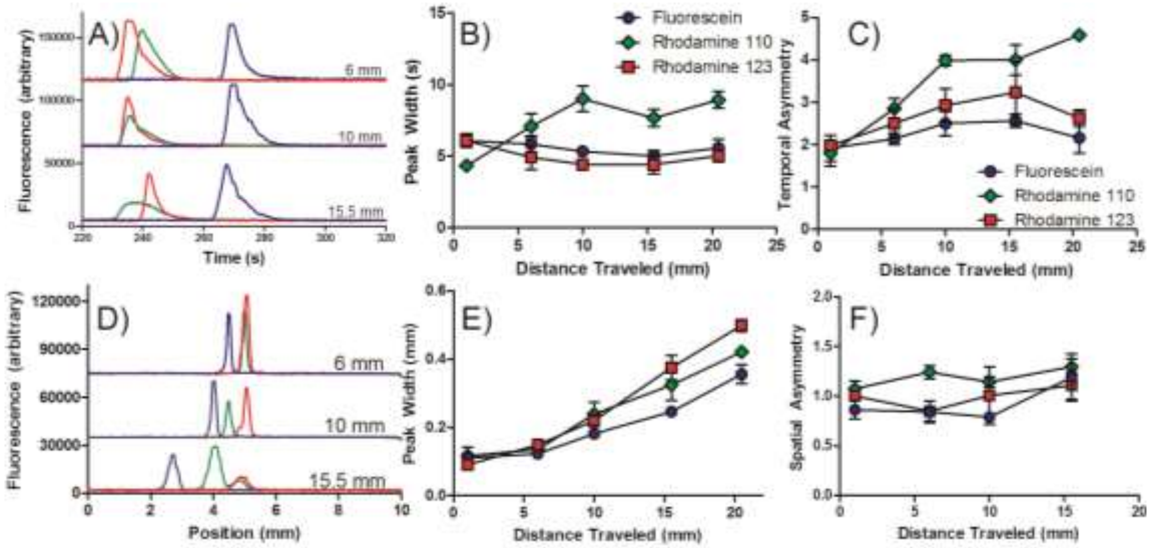

Figure 3.6. (A) Extracted chromatograms of rhodamine 110 (green), rhodamine 123 (red), and fluorescein (blue) measured in the µFFE separation channel 6.0, 10.0, and 15.5 mm from the sample inlet. (B) Temporal peak widths (half height) for fluorescein (blue circles), rhodamine 110 (green diamonds), and rhodamine 123 (red squares) at increasing distances from the sample inlet in the separation channel. (C) Temporal asymmetry of fluorescent dyes. (D) Extracted µFFE linescans at 6, 10, and 15.5 mm from the sample inlet. (E) Spatial peak widths (half height) for the same dyes at increasing distances from the sample inlet. (F) Spatial asymmetry determined from extracted linescans. Error bars are the standard error of the mean (n=3).

3.4.4 Temporal Asymmetry

Using the extracted chromatograms, adsorption was further investigated by determining the change in temporal asymmetry of the fluorescent dyes as they entered, and at various points along the separation channel. As shown in Figure 3.6C, analytes asymmetries were shown to increase by 0.3, 2.8, and 0.6 for fluorescein, rhodamine 110, and rhodamine 123 respectively. This indicates minimal surface adsorption as fluorescein and rhodamine 123 progress through the separation channel, and moderate adsorption for rhodamine 110. Figure 3.6A shows the extracted chromatograms as the 3 dyes transit down the separation channel. It can be seen visually that the dyes start initially broadened and do not significantly increase over the course of the separation channel. The initial asymmetry for all species is attributed to the elution off the nLC column as the analytes adsorb to the silica capillary used to introduce the sample. This asymmetry is maintained through the interface into the µFFE separation channel, which is supported by the similarity in peak shapes before and after the sample inlet (see Figure 3.4).

Most significantly, rhodamine 110 asymmetry increased from 1.8 to 4.6, for a 2.6x increase in the neutral ABS device. In previous glass devices, the asymmetry for rhodamine 110 stayed fairly constant around 2.0. The increased asymmetry in the ABS device is likely due to the neutral nature of the ABS surface and the zwitterionic rhodamine 110 interacting more than rhodamine 110 would in a negatively charged and hydrophilic glass device. In the previous glass µFFE device, a 1.75x increase in peak asymmetry was seen for rhodamine 123 while fluorescein and rhodamine 110 peak asymmetries stayed fairly constant. This further exemplifies the decrease in surface adsorption of rhodamine 123 in the ABS device.

3.4.5 Spatial Peak Widths and Asymmetry

Figure 6D-E shows the spatial dimension in the ABS device, linescans were generated for each fluorescent dye at various distances along the µFFE separation channel. The nearly linear increase in peak widths as the dyes traverse the separation channel indicates broadening due to diffusion and hydrodynamic broadening as predicted by Equation 1.1. The spatial asymmetries are also shown to be consistently around 1.0 for all analytes in Figure 3.6F. As described previously for µFFE devices, surface interactions should not change the spatial positioning, width, or asymmetry, as the analyte crosses the detection zone.[79] This is confirmed for rhodamine 110 in the ABS device as its moderate surface adsorption did not affect the spatial dimension of the separation.

3.4.6 Protein Surface Adsorption

Surface interactions between the fluorescent dyes and ABS channels were shown to be minimal. To further test the adsorption of the ABS device, proteins were explored. P503 labeled myoglobin and cytochrome c are analytes that are known to adsorb strongly to glass surfaces.

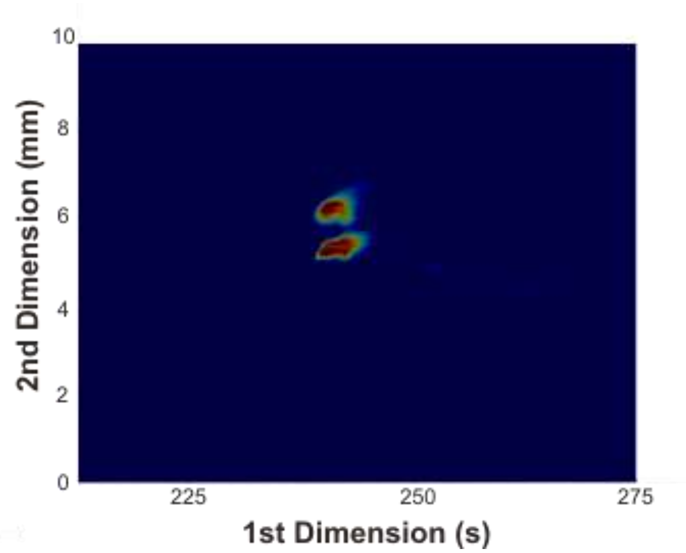

Figure 3.7. 2D nLC × µFFE separations of Chromeo p503 labeled myoglobin (top) and cytochrome c (bottom). Detection was performed in the µFFE separation channel 20.5 mm from the sample inlet.

Figure 3.7 shows a 2D nLC × µFFE separation of myoglobin and cytochrome c. The separation in the ABS device was performed with the same separation conditions as the fluorescent dyes. No surface coatings or buffer additives were necessary. The proteins were shown to adsorb minimally and were desorbed fully within 30 s after the peak initially reached the detector. Figure 3.8A shows the extracted µFFE linescan of myoglobin and cytochrome c at 20.5 mm from the sample inlet. The proteins were nearly fully resolved in the µFFE separation dimension and the peaks were reasonably symmetric. Figure 3.8B shows the temporal dimension of the 2D nLC × µFFE protein separation extracted at 20.5 mm. Some asymmetry is seen for cytochrome c, but is still fully desorbed in less than 30 seconds. Myoglobin showed little asymmetry and the peak width was less than 15 seconds. In glass µFFE devices, both myoglobin and cytochrome c adsorbed nearly irreversibly to the surface.[79] After 20 minutes, the signal had still not returned to baseline and a long rinse with NaOH was necessary to clear the glass channel of adsorbed proteins.

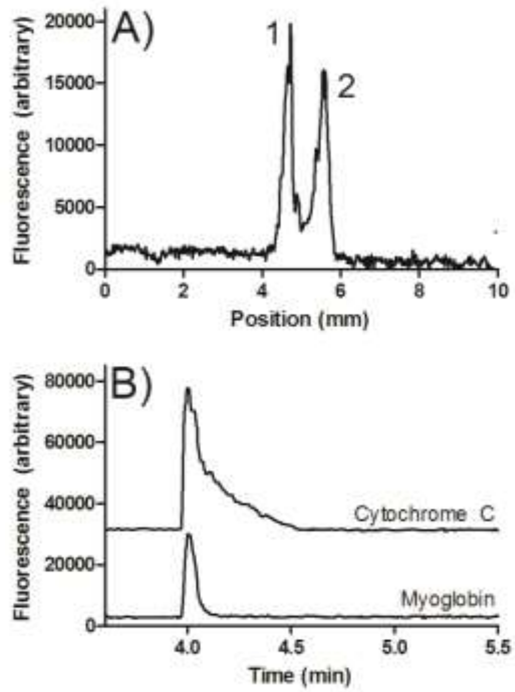

Figure 3.8. (A) Extracted µFFE linescan of Chromeo P503 labeled cytochrome c (1) and myoglobin (2). (B) Extracted chromatograms recorded in the µFFE separation channel 20.5 mm from the sample inlet.

This drastic decrease in adsorption compared to the glass device is attributed to the neutral surface of the 3D printed ABS device. Without a negative device surface charge, the positively charged portions of proteins no longer interact strongly with the surface. Myoglobin and cytochrome c have isoelectric points of 7.3[108] and 10[109] respectively resulting in their cationic nature, and adsorption to glass surfaces. The ABS plastic is also slightly hydrophilic,[106] and an increase in hydrophilicity has been shown to reduce non-specific protein binding of hydrophobic regions in other polymeric devices.[102,103] The presented device required no surface modifications to achieve its hydrophilicity, unlike in PDMS devices which require pretreatment. Fabrication of this device results in no need for surface modification, such as polymerization or coating the ABS device, or the need to add harsh chemicals to the buffer to limit surface adsorption. Also of note, only modest spatial asymmetry is observed in the μFFE dimension. This can be attributed to the heterogeneity of the protein structure or the labeling efficiency.

3.4.7 2D nLC × μFFE BSA Digest Separation

Elimination of surface adsorption in 2D separations is necessary for successful 2D separations. If there is significant surface adsorption the resolution of the separation will decrease, resulting in lower peak capacity separations. To demonstrate the capabilities of the 3D printed 2D nLC × μFFE, a more complex peptide sample was analyzed. A P503 labeled tryptic digest of BSA was prepared. This sample was chosen in order to compare it to a similar BSA digest run on a glass device setup that was previously used to demonstrate the utility of μFFE as a second dimension for multidimensional analysis.[40] Shown in Figure 3.9 is the separation of the BSA digest on the ABS 3D printed nLC × μFFE coupling. ~30 peaks are observed in a 5 min separation window. The peptides do not appear to adsorb in the temporal dimension. Most notably, this separation was achieved without the use of any buffer additives or channel coatings. In glass µFFE devices a PEO coating and 8 M urea buffer additive were necessary to reduce surface adsorption enough to perform the separation. For the 3D printed device, the same buffer was used for fluorescent dye, protein, and peptide separations. Furthermore, no channel coatings were ever needed during any separations. In glass devices, these additions were necessary to reduce surface adsorption enough for resolution of analytes in the temporal dimension. Elimination of the surface adsorption allows for nice 2D separations, lack of resolution in the temporal dimension is detrimental and can lend a 2D separation useless if surface adsorption is not eliminated.

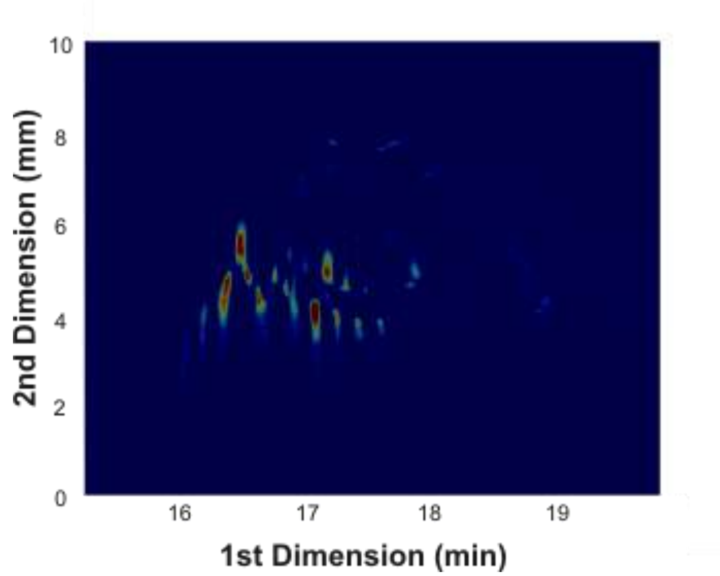

Figure 3.9. 2D nLC × µFFE separations of Chromeo p503 labeled BSA digets. Detection was performed in the µFFE separation channel 15.5 mm from the sample inlet.

3.5 Conclusions

The use of ABS as a substrate for µFFE separation device overcomes previous surface adsorption setbacks in 2D nLC × µFFE separations. The neutral ABS device does this without the need for buffer additives, surface coatings, or lengthy flushing processes. Cytochrome c and myoglobin were separated and desorbed from the 3D printed ABS device in less than 30 seconds, compared to >20 minutes and the need for an NaOH wash in a glass device.[79] A complex 2D separation on a 3D printed device was also performed without the need for coatings or buffer additives. Minimal surface adsorption was observed on a device that was produced in less than 2 days, for ~$0.20 of non-reusable parts. The ABS – 3D printed device demonstrated the neutral and hydrophilic nature of the ABS plastic can overcome the extreme surface adsorption in the temporal dimension of glass microfluidic devices. ABS also could be used in other thermoplastic fabrication schemes, such as hot embossing or injection molding, for devices that want to reduce cationic analyte adsorption. Furthermore, other thermoplastics with varying surface properties could theoretically be 3D printed specific to the type of sample to be analyzed and desired detection method, with the goal of reducing surface interactions.

Chapter 4

Coupling Micro Free-Flow Electrophoresis with Mass Spectrometry

4.1 Summary

Identification of analytes utilizing µFFE has been a difficult problem to solve due to the spatial nature of the separation. Detection methods in µFFE have been mostly limited to LIF. This method does not allow for identification of the sample without the need for sample spiking, or fraction collection and subsequent mass spectrometric detection. Furthermore, µFFE does not lend itself well to fraction collection as only a few outlets are feasible on a microfluidic device, and the volumes produced are small. This chapter details production of an open edge µFFE device that allows for a separated sample to flow off the edge of the device and to be deposited on a polyvinylidene difluoride (PVDF) membrane for sample concentration, clean up, and mass spectrometric analysis. A theoretical open edge device was evaluated with COMSOL and found to have stable pressure throughout the device, even with the edge open to atmospheric pressure. Stream stability tests have been performed in an open edge glass device, and further exemplified the stability of the flow in open edge devices. Three fluorescent dyes have been separated in the glass open edge device, and shown that the open edge does not affect the voltage or separation in the device. Utilizing the glass open edge device, BSA has been deposited directly from the device onto the PVDF membrane. A protein stain was used for visualization of the immobilized protein on the membrane. Further work has been done on manufacturing an ABS device by FDM to improve on the open edge design, where the glass fabrication limited the design possibilities. Modifications have been made to the ABS device that were not possible with the glass device, including tapering the edges of the device. This reduces the number of pressure points and non-uniform contact with the membrane, which was observed when using a glass device. The utility of the 3D printed devices has been shown in the ability to modify the device daily to work towards achieving a device that can interface to the PVDF membrane, and MALDI-TOF/TOF.

It has been demonstrated that proteins can be desorbed from PVDF hydrophobic membranes. Myoglobin and leptin have been pipetted onto the PVDF membrane, ionized, and detected directly from the membrane by MALDI-TOF/TOF. The ideal matrix concentration has also been determined to be ~0.008 µg/mm through systematic analysis of protein and co-matrix mass per area concentration on the PVDF membrane. Sample has also been deposited from both glass and ABS devices onto PVDF membranes. Work is still needed for efficient transfer from the device to the membrane without loss of resolution.

4.2 Introduction

Analyte detection in many microfluidic devices is limited due to the small nature of the devices. Short path lengths and small sample volumes make detection difficult. These problems have been overcome in many microfluidic devices and detection methods such as UV, IR, LIF, and Raman have all be utilized in various microfluidic devices.[15] µFFE proves to be more difficult to detect on than other microfluidic devices due to the spatial nature of the separation. For this reason, fluorescence detection is the main detection method used for µFFE, and specifically LIF is utilized frequently. The ability to expand the laser into a line allows detection over an area on the device.

Identification of analytes on many microfluidic devices has also been achieved by coupling the microfluidic devices with mass spectrometry. This coupling has proven difficult for μFFE devices. Coupling to a mass spectrometer allows for identification of analytes without the need for fraction collection, sample spiking, or other methods used to identify analytes after separation. Many couplings of on chip separations to mass spectrometry have been reported. The Ramsey group has produced a microfluidic CE device that couples directly to a mass spectrometer by producing an electrospray at the corner of the device.[110] A glass fabricated nanospray emitters on a microfluidic device has also been reported by Belder *et al.*[111] Many couplings to MALDI have also been noted. Lee *et al.* coupled a PMMA bioreactor to a MALDI plate that had been spin coated in nitrocellulose polymer covered in MALDI matrix.[112] The Devoe group reports the automated spotting of sample onto a customized MALDI plate from eight parallel micro channels.[113] Zhang and Caprioli demonstrate the deposition of analytes from a CE capillary directly onto a membrane pre-coated with matrix.[114] These setups all utilize preparation and separation techniques that end in a single outlet. Due to this feature, there is minimal loss of resolution in directly interfacing the outlet, making them amenable to electrospray emitter setups, or easy depositions onto MALDI plates from a capillary. Benz *et al.* have demonstrated an example of μFFE coupled with mass spectrometry through a nanospray emitter.[115] This setup utilized the μFFE device as a micropreparative FFE fractionation directly into a mass spectrometer. Flow in the device was dictated such that the sample streams produced during the separation were effectively scanned and individually sent to a single outlet from a nanospray emitter and into the mass spectrometer for identification. This exemplifies the difficulty in μFFE couplings. The end of a μFFE separation terminates in a planar channel so either sample is lost, as demonstrated in the previous example, or outlets need to be integrated for fraction collection. Integration of outlets renders the separation less powerful because few outlets are feasible on a μFFE chip, which could cause multiple peaks to be combined through a single outlet. For this reason, a means to directly couple the full separation channel to a mass spectrometer is highly desirable.

There are many ionization methods in use for introduction of analytes into mass analyzers. MALDI or Desorption Electrospray Ionization (DESI) is predicted to be the most likely ionization method to work for μFFE couplings due to their ability to image a 2D space. Methods like ESI and nanospray emitters ionize a stream of analyte from a capillary or microchannel, which is not amenable to use with the planar μFFE channel. Advances in MALDI and DESI have led to the ability to image an area, and both have been used for imaging tissues.[116]

3D printing, specifically FDM, has been shown to be a reliable, robust fabrication method for developing novel μFFE devices. Prototyping of new devices is possible in a fraction of the time compared to glass manufacturing methods. There is also more creative freedom for the user when designing device specifications due to the ease of modifications associated with using thermoplastics instead of glass. By utilizing FDM it is plausible to develop a μFFE device that could indirectly couple to a mass analyzer, without under sampling or decreasing resolution.

In the following chapter we assess the feasibility of an open edge μFFE device for use in depositing sample directly from the separation channel on to a PVDF membrane for subsequent MALDI-TOF/TOF protein analysis (see Figure 4.1).

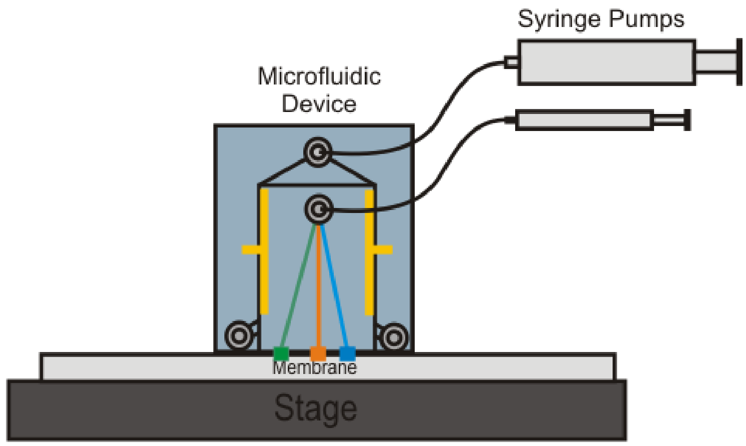

Figure 4.1. Experimental setup for coupling μFFE to MALDI-TOF/TOF. The analyte is introduced into the separation channel and carried through the device by pressure driven flow. Analytes are separated by applying a voltage lateral to the flow. The separation then ends by flowing off the μFFE device and onto a hydrophobic membrane. The membrane can then be introduced into a MALDI-TOF/TOF, and the sample ionized off the membrane.

4.3 Experimental

4.3.1 Chemicals and Reagents

All solutions were made with deionized water (18.3 MΩ; Millipore, Bedford, MA) and filtered with a 0.22 μm nitrocellulose membrane filter (Fisher Scientific, Fairlawn, NJ). μFFE separation buffer contained 300 μM Triton X-100 and 25 mM HEPES all of which were purchased from Sigma-Aldrich (St. Louis, MO). The pH of the buffer was adjusted to 7.00. Stock solutions of rhodamine 123, rhodamine 110 chloride and fluorescein (Sigma-Aldrich) were prepared at varying concentrations, in water. Stock solutions of myoglobin (equine skeletal muscle, Sigm a-Aldrich) and leptin (Sigma Aldrich) were prepared in 10 mM $NaHCO_3$ (Mallinckrodt, Paris, KY) in water at concentrations of 1.0 mg/mL.

Immobilon P^{SQ} transfer membranes (Millipore) were used for protein deposition from the μFFE device. Pierce protein staining kit (Thermo Fisher Scientific) was utilized to visualize and verify that the protein was captured on the membrane after deposition. Sinapinic acid was used as a matrix for MALDI-TOF/TOF at 10 mg/mL in 50/49.9/0.1 – ACN/H_2O/TFA. Piranha solution (2:1 H_2SO_4/H_2O_2) (Ashland Chemical, Dublin, OH) was used to clean glass wafers and etch Ti. (CAUTION: Piranha solution reacts violently with organic materials; it must be handled with extreme care.) GE-6 (Acon Technologies, INC., Pittson, PA) was used to etch Au. Concentrated HF (49%) (Ashland Chemical) was used to etch glass wafers. Silver conductive epoxy (MG Chemicals, Surrey, BC Canada) was used to make electrical connections to the glass μFFE device. Clear ABS (RepRapper, Hong Kong, China) was used for all 3D prints. 250 μm diameter Pt wire (Sigma Aldrich) was used for electrodes in the 3D printed device. Acetone (Fisher Scientific) was used to produce acetone vapor for smoothing and bonding of 3D printed layers. Epoxy (Loctite, Westlake, OH) was used to hold Pt wires in place and seal the electrode access holes.

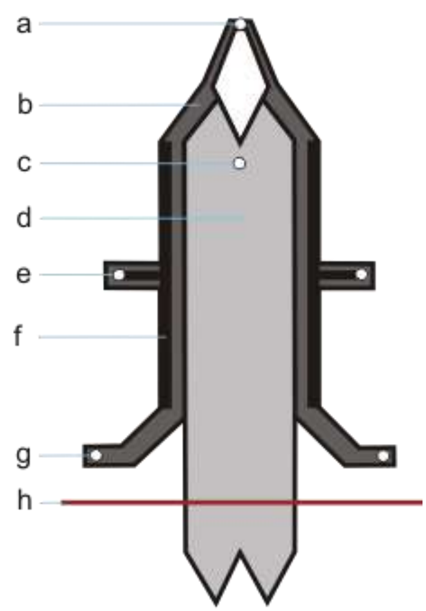

Figure 4.2. μFFE device design. (a) buffer inlet, (b) electrode channel, (c) sample inlet, (d) separation channel, (e) electrode attachment, (f) electrode, (g) buffer outlet, (h) cut line.

4.3.2 Glass μFFE Design and Fabrication

Figure 4.2 shows the design of the glass open edge μFFE device including where the device is cut to allow the separation channel to flow to the edge of the device. Fabrication followed procedures similar to Figure 1.3 and Chapter 2.[10,28,91] Figure 4.3A shows the fully fabricated glass device. The separation channel was elongated to allow for the device to be diced producing the open edge. This was achieved by a double exposure of the separation channel during fabrication. The separation channel was exposed once for 4 seconds and then the mask moved down to elongate it and exposed again. No loss in features was observed due to this added step. To facilitate better contact with the deposition membrane, the edge of the open separation channel was ground with a hand held dremel rotary tool (Dremel, Racine,WI) in an attempt to smooth and eliminate defects from machining.

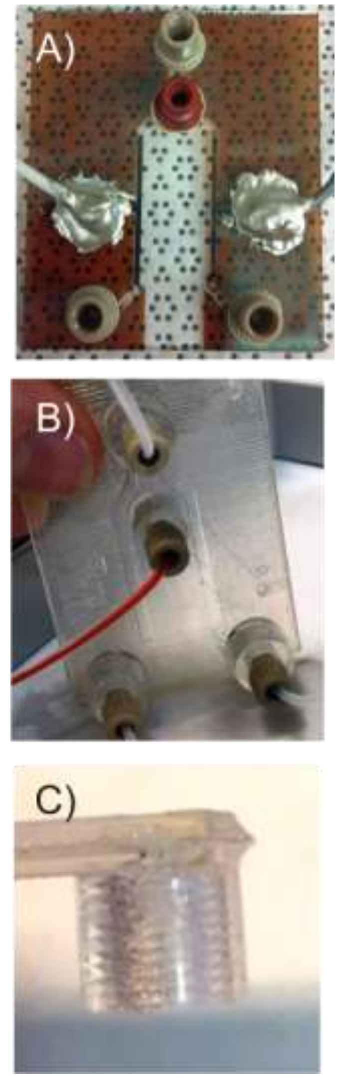

Figure 4.3. Images of a (A) glass open edge μFFE device, (B) 3D printed open edge μFFE device with electrode channels, and (C) side view of the tapered edge of the 3D printed device.

4.3.3 3D Printed μFFE Design and Fabrication

A simplified device was made to test the deposition of proteins from the ABS μFFE device. Modifications include the removal of electrodes and the electrode channels, and tapering the edge of the device (shown in Figure 4.3C). Figure 4.3B depicts an open edge μFFE device with electrode channels 3D printed using clear ABS plastic. Features of the top and bottom layers of the device were designed using AutoDesk Inventor (see Figure 4.4). The CAD included 345 μM deep electrode channels and an 80 μm deep × 3 cm long × 1 cm wide separation channel. The fabrication followed procedures similar to those previously reported in Chapter 2.[107]

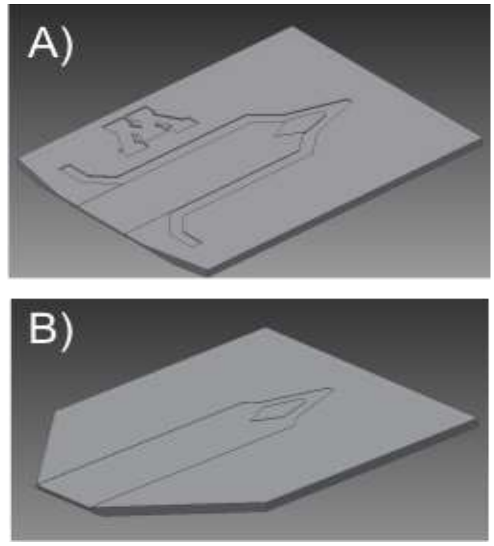

Figure 4.4. CAD images of the feature side of the open edge device with (A) electrode channels and (B) without electrode channels. The edges are tapered in both CAD drawings to reduce the amount of contact with the membrane so that only the separation channel comes in contact during deposition.

4.3.4 μFFE Separation and BSA Deposition onto PVDF

Separation buffer or water was pumped into the devices at a flow rate of 0.5 mL/min for the glass devices and 0.13 mL/min for the ABS device. Flow was reduced in the ABS device to more closely match the linear velocity of the glass device due to the elimination of the electrode channels. Sample was introduced into the separation channel at 1 μL/min (Separation buffer pump: Model # 55-2222, Harvard Apparatus, Holliston, MA; Sample pump:

New Era Pump Systems, Model # NE-300, Farmingdale, NY). During µFFE separations, the right electrode was grounded and varying voltages were applied to the left electrode using a power supply (PS310, Stanford Research Systems INC, Sunnyvale, CA). Tefzel® Tubing (1/16" OD × 0.040", IDEX Health and Science, Oak Harbor, WA) was connected directly to the Nanoports on the glass device, or printed access ports on the ABS µFFE device using modified commercially available fittings (10-32 and 6-32 coned finger tight ferrules, IDEX, Science, Oak Harbor,WA) and o-rings. A Snap i.d. 2.0® (Millipore) was utilized to pull a vacuum on the hydrophobic PVDF membrane during depositions. The setup was layered from bottom to top with a Snap i.d. blot holder, fine mesh wire, support filters, PVDF membrane, and then a plastic sheet over the top only allowing access to a small portion of the PVDF membrane. All of these layers were housed in the Snap i.d holder. This setup allowed for support underneath the membrane when the device was set on it, and an increased vacuum in the desired area.

4.3.5 µFFE Detection and Data Collection

An AZ 100 stereomicroscope (Nikon Corp., Tokyo, Japan) mounted with a 100 W X-Cite fiber-optic metal halide lamp (Nikon Corp.) and Cascade 512B CCD camera (Photometrics, Tucson, AZ) was used for fluorescence imaging. The microscope was equipped with an Endow GFP emission filter cube (Nikon Corp) containing two bandpass filters (450-490 nm and 500-550 nm) and a dichroic mirror (495 nm cutoff). A 1.6× objective was used for collection with a 0.7× CCD camera lens. Analyte detection was performed using 0.75× zoom to image the 1 cm wide separation channel at various distances downstream from the sample inlet. For LIF detection, a 150 mW beam from a variable power 488 nm 150 mW diode pumped solid state laser (Sapphire, Coherent, Santa Clara, CA) was expanded to a ~2.5 cm wide by ~150 μm thick line across the glass μFFE separation channel directly below the microscope objective.

4.3.6 MALDI Analysis

Proteins were spotted onto PVDF membranes using a 1-10 μL pipette. Volumes ranged from 1-4 μL and were deposited 1 μL at a time while a vacuum was applied to the membrane by a Snap i.d. device. 1-3 μL sinapinic acid matrix, deposited 1 μL at a time, was then deposited on top of the spotted proteins with no vacuum applied, and the membrane heated on the MALDI spot plate on a hot plate to facilitate crystallization of the matrix. The PVDF membrane was affixed to the MALDI spot plate using copper tape. Proteins were analyzed by a

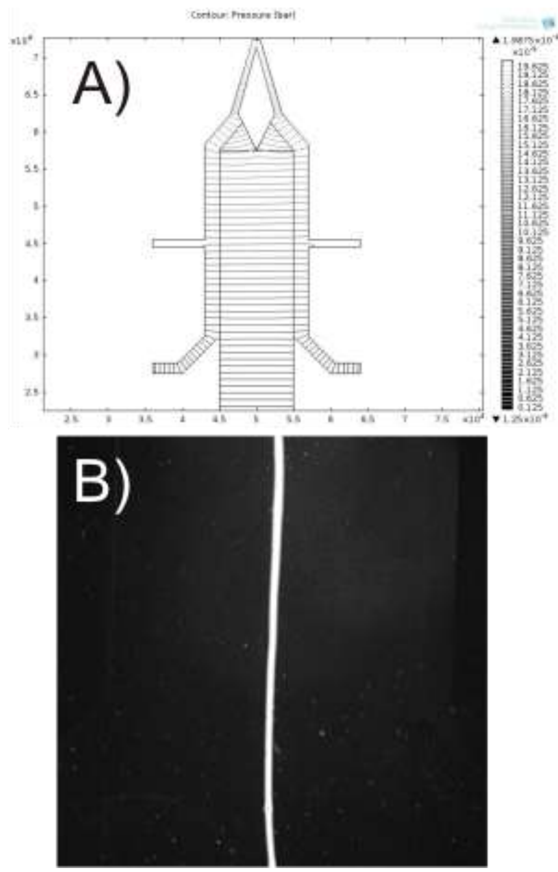

Figure 4.5. (A) COMSOL simulation of the pressure contour map in an open edge μFFE glass device. (B) A stream profile of 1 mg/mL FITC-BSA with 0V applied, demonstrating the stability of the flow in the open edge glass μFFE device.

MALDI TOF/TOF 5800 (Sciex, Ontario, Canada) in linear mid mass mode with a laser intensity of 5500-6500 (arbitrary units), and 200 shots per sample, with a sample taken every 200 μm across the image. A range of 14,000 – 18,000 mass-to-charge ratio (m/z) was analyzed. After imaging the area of the PVDF membrane, the data was then processed to show the specific m/z values of the desired proteins over the imaged area.

4.4 Results and Discussion

4.4.1 Glass Open Edge Device

Prior to fabrication, the fluid dynamics of the open edge device was mathematically simulated using COMSOL. The simulated pressure throughout the separation channel was not found to be affected by opening the separation channel of the device to ambient pressure, shown in Figure 4.5A. Upon verifying that the flow would likely not be altered due to the necessary modification, the device was fabricated in glass and the edge diced to allow the separation channel to extend to the edge of the device. Figure 4.3A show the fully fabricated glass device, and Figure 4.5B demonstrates the lack of flow irregularities in the glass open edge device by streaming BSA into the device at 0 V. The device was further characterized by separating

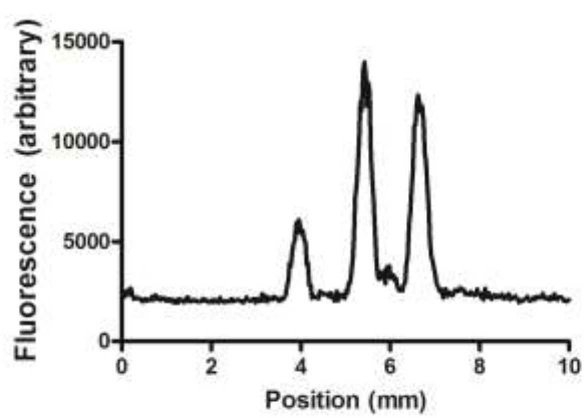

Figure 4.6. Separation of fluorescein, rhodamine 110, and rhodamine 123 (left to right) at 100 V in an open edge glass μFFE device.

fluorescein, rhodamine 110, and rhodamine 123 to verify the device was fully functional. This demonstrated the ability to apply a voltage with the open edge modification. The linescan of the three dye separation is shown in Figure 4.6. All three dyes are baseline separated in the open edge glass µFFE device.

4.4.2 Deposition from Glass µFFE Devices onto a Hydrophobic Membrane

Proteins were deposited from an open edge glass µFFE device on to PVDF hydrophobic membranes. By depositing proteins directly onto a hydrophobic membrane, across the whole channel, the separation is maintained. This is unlike other methods that fractionate the flow into outlets, or scan across the separation channel, effectively undersampling the separation.

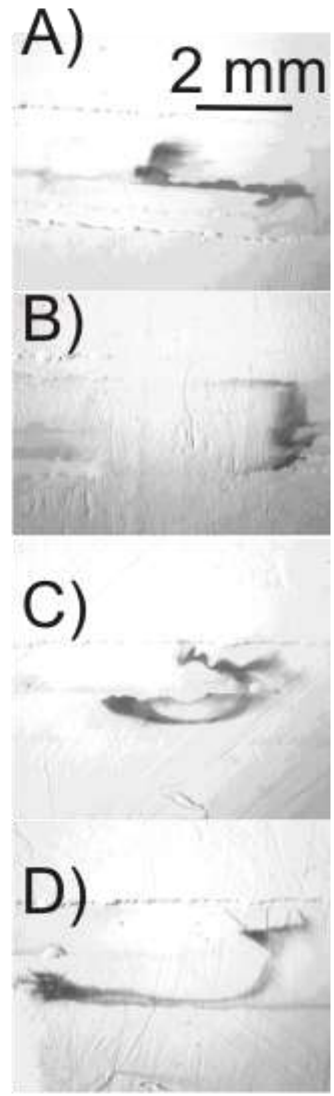

Figure 4.7. Shown are various depositions of 1 mg/mL BSA from an open edge glass device at the same flow rate. The membrane and protein were stained and images with a light microscope. Various artifacts can be seen due to the positioning and nature of the open edge glass device.

Protein deposition was achieved by setting up the Snap i.d. device as described in Section 4.3.4. This method was utilized in order to allow enough of a vacuum to be pulled on the PVDF to not have excess running buffer and sample flow onto the membrane during deposition. If any sample wasn't immediately passed through the membrane, the proteins would not concentrate in one location. Contact between the membrane and device was done by setting the device onto the membrane and then either taping or holding in place so it did not shift during depositions. After the deposition, the membranes were stained with a protein staining kit to image the deposited proteins. Many modifications to the device were necessary to make this possible, and even with these modifications there was a lot of inconsistency with the deposition method. Figure 4.7 shows various attempts at depositing BSA from a glass device, onto the hydrophobic membrane. These attempts failed due to the difficulty in aligning the glass device on the PVDF membrane. Figure 4.7A demonstrates the analyte traveling along the cracks produced during the dicing stage of the fabrication as it exits the device. Figure 4.7 B-C demonstrate what happens if the device is uneven, either tilted during deposition, or not making full contact with the membrane, allowing the analyte to pool along the base of the open edge device. Figure 4.8, demonstrates a more successful deposition. BSA was deposited on the PVDF membrane from the glass open edge microfluidic device, producing a deposition size of approximately 1.4 x 1.5 mm. The size of the deposition is significantly larger than would be expected from a 20 micron separation channel. This improvement was partially attributed to grinding the edge of the device with a dremel tool in order to smooth the edge of the device. This eliminated bumps and cracks

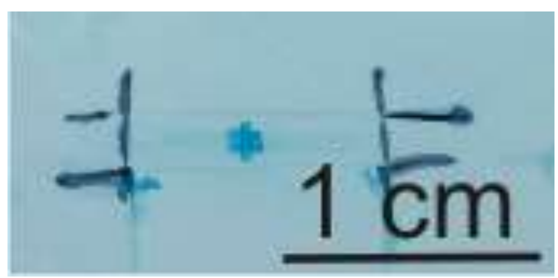

Figure 4.8. Deposition of 1mg/mL BSA from glass open edge device onto a PVDF hydrophobic membrane. Black lines indicate the width of the device (2.2 mm) and the length of the separation channel (1 cm). The blue background is due to the protein stain utilized to visualize the BSA on the membrane. The spot deposition was 1.4 x 1.5 mm

created when the device was diced. Even with these improvements, more work is still needed and depositions were not very consistent.

4.4.3 Glass Fabrication Problems

Using glass fabrication there are many limitations to creating new interfaces. Glass is extremely rigid both physically and in its manufacturing processes. In manufacturing the glass device, there is not much creative liberty taken during the process which results in only small modifications that can be made, such as the lengthening of the separation channel that allowed for dicing the device and opening the separation channel to the edge of the device. There were also few post fabrication modifications that could be made other than grinding the glass near the separation channel to try to decrease the amount of surface coming into contact with the deposition membrane, shown in Figure 4.9. While this helped smooth the edge of the device and resulted in more even contact with the trapping membrane, there were risks of further cracking of the device, and clogging the separation channel. The physical rigidness of glass also made dicing the devices very difficult. With the wide 1 cm separation channel, and the amount of force needed to dice the device across the separation channel, it was common for the device to break during this final step of production. This led to massive amounts of lost time, and money. To overcome this, new 3D printing fabrication methods were investigated. Specifically leading to the 3D printed fabrication method described in Chapter 2 and the characterization of the surface adsorption properties of the new ABS devices, discussed in Chapter 3.[107]

4.4.4 3D Printed μFFE Device

A ABS 3D printed device was manufactured with the separation channel ending in an open edge to the side of the device. Electrode channels were removed from the device to simplify the device and allow for fewer variables when improving the deposition method (see Figure 4.4B). The edge of the device was also tapered 45 degrees on either side of the separation channel, along the edge of the device, to further reduce the amount of contact with the membrane during deposition (see Figure 4.3C). Bonding was successful using the previously described acetone vapor bath in Chapters 2 and 3,[107] and did not result in the end of the separation channel closing, or any leaks in the device. It has been show that the analyte can flow off of the 3D printed device and deposited on a PVDF membrane, shown in Figure 4.10. Depositions have also been noted to be more consistent than when using a glass device and no artifacts of contact with the membrane observed due to the modifications that are possible with 3D printing. Most notably, the tapering of the edges of the device to reduce contact points,

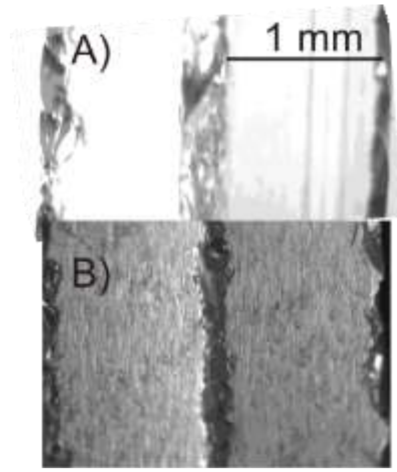

Figure 4.9. 20x image of the open edge separation channel of a μFFE device. Comparison (A) before and (B) after grinding of open edge to facilitate better contact with membrane.

Figure 4.10. Deposition of 1 mg/mL BSA combined with red food dye from an open edge 3D printed device. Water was used as a buffer and pumped at 0.13 mL/min in the modified, no electrode channel devce. Resulting deposition spot was ~ 1 mm x 3 mm.

shown in Figures 4.3C and 4.4, have improved the robustness of the method. Improvements are still needed in the efficiency of the deposition from a fully functional device, and application of a voltage.

4.4.5 MALDI-TOF/TOF Analysis of Proteins on PVDF Membranes

To assess the feasibility of desorbing proteins from hydrophobic membranes using a surface ionization technique, myoglobin and leptin were deposited onto various membranes 1 µL at a time with a pipette. Ionization of the proteins directly from the membrane was attempted by desorption electrospray ionization (DESI) and MALDI. DESI was attempted first, and a successful ESI charge envelope characteristic of myoglobin was seen off of a membrane (see Figure 4.11). Unfortunately, the reliability

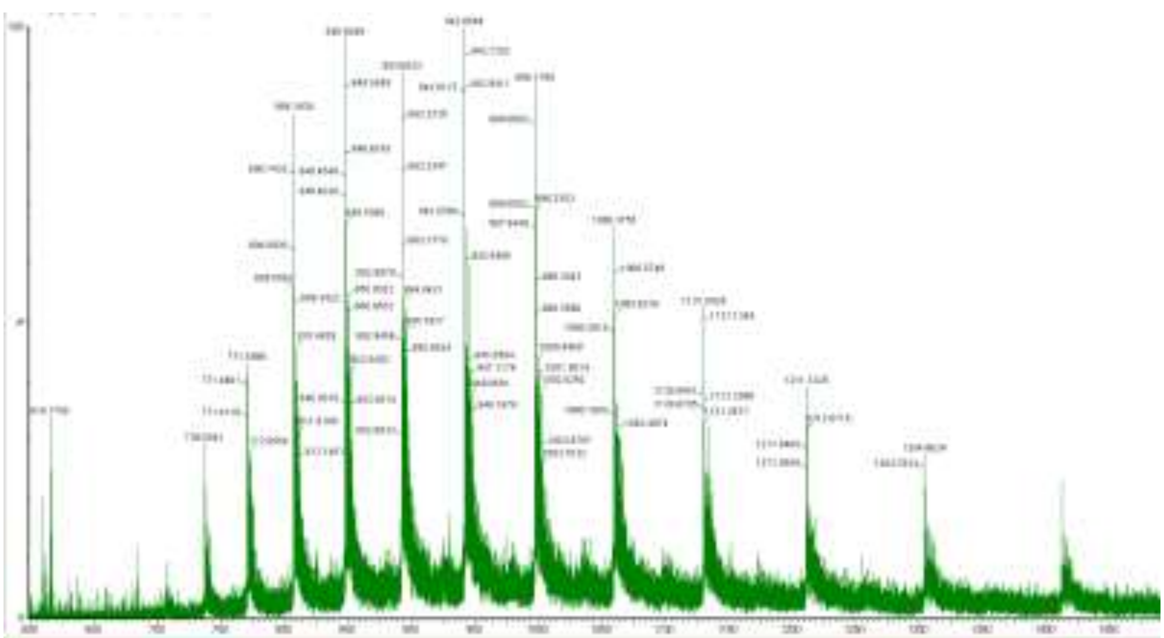

Figure 4.11. 1 µL of Myoglobin was spotted onto a hydrophobic membrane at a concentration 1 mg/m and then DESI-MS performed on the spot. A charge envelope characteristic of myoglobin was produced.

of the method was poor. In order to get a successful ionization, the DESI source had to be in perfect alignment, which could take hours to succeed at, and only work one time in a day, on a good day.

MALDI imaging was then investigated and determined to be much more robust. Proteins were able to be ionized from membranes with no need to align or tune the ionization, unlike with DESI. Furthermore, the spatial resolution of DESI is typically around 250 µm according to the manufacturer. Meanwhile, the spatial resolution for MALDI imaging is stated down to 50 µm according to the manufacturer. That increases the number of samples possible across a 1 cm separation channel from 40 for DESI to 200 samples for MALDI.

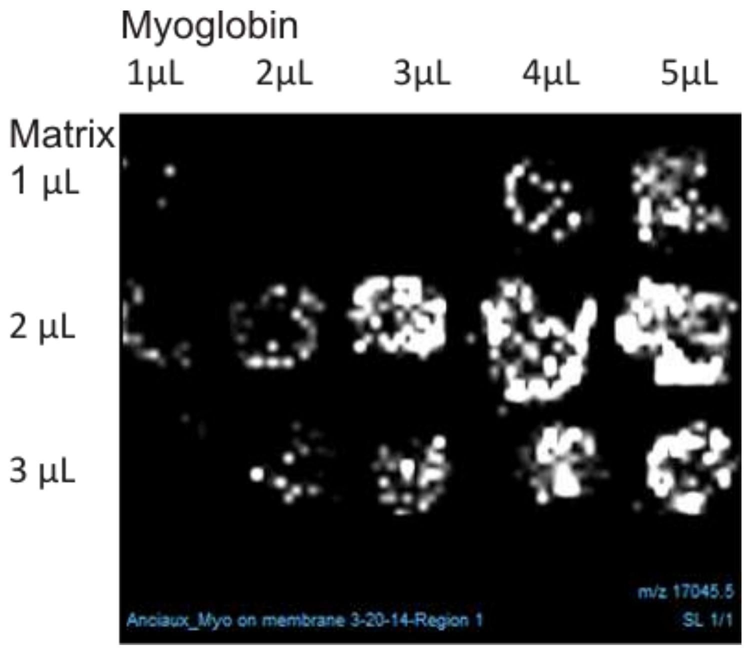

Figure 4.12. Deposition of 1-5 µL of 1 mg/mL myoglobin onto PVDF membrane with 1-3 µL of matrix. It can be seen that the amount of matrix plays a large part in the observed signal of myoglobin.

Myoglobin and leptin were both successfully ionized from the PVDF membrane by MALDI. Figure 4.12 demonstrates the effect of the mass deposited of the proteins and co-matrix. 2 µL of co-matrix was determined to be the best composition for the ~2-3 mm spot size produced by pipetting. It was also determined that heating of the membrane with protein and matrix on it was necessary to facilitate crystallization of the matrix. Without heating, there was visibly less crystallization of the matrix and no signal seen. Figure 4.13 depicts the MALDI-TOF/TOF analysis of Leptin. Leptin has a molecular weight of ~16 kDa.

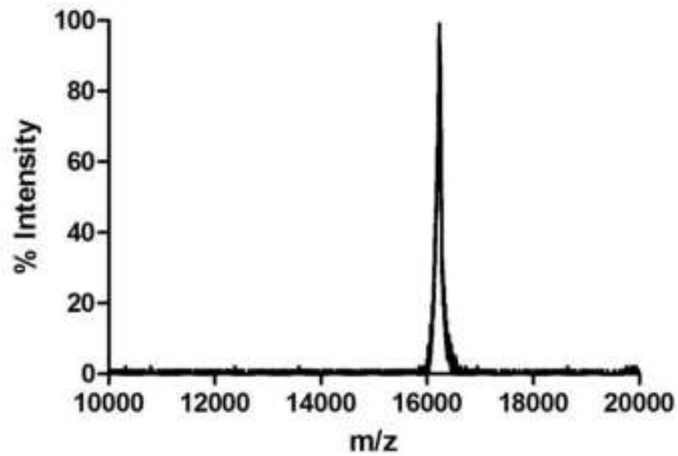

Figure 4.13. Deposition of 2 µL of 1mg/mL leptin with 2 µL matrix applied and heated. The m/z signal of just over 16 kDa is indicative of leptin.

4.5 Conclusions

Functional devices in both glass and ABS have been developed that allow the sample to exit the device through the open edge. Flow has been shown to be steady in glass devices and separations unaffected by the open edge. Deposition of the analyte stream onto the PVDF membrane has been successful, although only in a limited capacity. It is necessary to improve the deposition of the analyte stream onto the membrane, most likely through improved application of a vacuum. MALDI-TOF/TOF has proved a reliable method for desorption of protein from PVDF membrane for myoglobin and leptin. Imaging of spatial regions is also possible and specific m/z monitoring allowing for selective identification of analytes.

Chapter 5

Summary and Future Work

5.1 Summary

Micro free-flow electrophoresis is a technique that is amenable to a variety of applications, largely due to the continuous nature of the sample introduction. The work presented in this thesis demonstrated a new fabrication technique that greatly reduces the cost and time associated with the production cycle of these devices. Through this reduction in cost, and especially time, it is now feasible to modify and apply this separation technique to many new applications. Huge steps have been made in advancing the detection and identification of the previous setup through the use of 3D printing and MALDI analysis, but more work here is needed. The deposition off of the 3D printed device while a voltage is applied still needs work, and a proof of concept.

In chapter 2, a new fabrication method was developed and validated. The first demonstration of 3D printing a µFFE separation device with a dimension on the microscale was achieved. The device was shown to be able to separate fluorescent dyes and proteins, with the limit of detection as low as 2 nM for rhodamine 110. The device was fabricated for less than $0.20 of non-reusable parts in less than two days. This is a 5,000+ fold decrease in cost, and nearly a 10 fold decrease in production time. This huge decrease in cost and time will allow for more creative freedom, and rapid prototyping of novel devices. Chapter 3 further developed the feasibility of using 3D printed microfluidic device though investigating the surface adsorption in the device. Surface adsorption can be a huge problem in microfluidics, leading to band broadening, and a reduction in the resolution of analytes. Surface adsorption can be difficult to overcome in glass devices, requiring harsh buffer additives, surface coatings, and extensive flushing of the device after simple separations. This chapter exemplified the use of thermoplastics such as ABS for manufacturing µFFE devices. The slightly hydrophilic, neutral nature of the 3D printed ABS is a great combination to nearly eliminate surface adsorption in the µFFE devices. It was shown that fluorescent dyes, peptides, and proteins did not adsorb to the surface of the ABS device. Temporal asymmetries and peak widths were compared to that of a glass device, and show to be unaffected by surface adsorption in the ABS device. This allowed for separation of the fluorescent dyes, peptides, and proteins, using the same buffer for all of them. No buffer additives, surface coatings, or extensive washes were needed after the separations as minimal surface adsorption was seen. Furthermore, the 2D coupling of nLC to µFFE was achieved and lends itself well to future 2D couplings with the 3D printed µFFE device.

This work demonstrates that fabrication of the device in chapter 2 and the surface characteristics determined in chapter 3 set this device up to be utilized for mass spectrometry couplings. Work in chapter 4 demonstrates that the open edge µFFE device has stable flow, and the ability to get analytes off of the device, onto a PVDF membrane shown to be possible. These analytes were also show to be able to be ionized directly from a hydrophobic membrane using MALDI-TOF/TOF.

5.2 Future Work

As stated in Chapter 1, µFFE can be operated in many different modes including ZE, IEF, ITP, and MEKC. The ability to select which mode the second dimension is simply by changing the buffer is ideal. Previously, µFFIEF has been difficult to implement as a second dimension in glass due to the constraints of the fabrication process, and the integration of many fluidic access ports. With the improvement in fabrication methods demonstrated in this manuscript, it is predicted that the production of a functional 3D printed µFFIEF devices is possible based off previous designs.

In Chapter 3, it was demonstrated that nLC could be coupled to the 3D printed µFFE device. Complex peptide separations were performed and many peaks fully resolved. Further work could be done on coupling to other sampling methods such as microdialysis, and other 2D couplings such as to CE. It took years to develop the nLC $\times$ µFFE coupling to a glass device due to the fabrication constraints. For the 3D printed ABS devices, once the methods were in place it took less than 2 weeks to implement new couplings. It is predicted that these methods will greatly increase the productivity and creativity of future work.

Finally, work is still needed to demonstrate the utility of µFFE coupling to MALDI-TOF/TOF. Work in Chapter 5 demonstrated the functionality of the device, its stable flow, and ability to get the analytes off of the µFFE device. Further work is needed to demonstrate the platform as fully functional.

5.2.1 µFFE Modes of Operation and 2D Couplings

The coupling of µFFE to other separation techniques has been a large area of study for the Bowser lab over the last 10+ years. Limitations have mostly been due to fabrication problems, such as defects created in the glass during the etching steps, and slow turnover of functional devices, or pressure issues that arise and cannot be easily fixed due to the rigid fabrication process. The validation of 3D printing as a new fabrication technique allows for rapid production of devices.

With 3D printing, a fully functional nLC × µFFE was demonstrated in Chapter 2, and the fabrication of the device took ~2 days. This coupling was achieved by introducing a capillary directly into the separation channel during the bonding step of the fabrication. Further work could be done to explore other possibilities of 2D couplings. This could include inserting a longer capillary into the 3D printed device, such that CE could be performed, and injected directly into the µFFE device, rather than coupling the capillary to nLC. Separations could then be performed by varying the modes of separation in the CE and µFFE. One could imagine performing ITP in the CE dimension and MEKC for the µFFE dimension. Furthermore, µFFIEF has been an area of interest as it is predicted that the peak capacity of the µFFE device could be improved by using µFFIEF. By the nature of IEF, analyte bands effectively focus and become more resolved the longer the separation goes, unlike in ZE or MEKC where the analyte bands broaden in an electric field due to diffusion and hydrodynamic broadening, shown in Equation 1.1.

By developing a device capable of µFFIEF, the peak capacity in the second dimension could be increased by nearly 50%, effectively increasing the separation power of a 2D separation. Previously µFFIEF devices have been very difficult to manufacture due to the large number of outlets needed, and the difficulty of prototyping new devices in glass. It would take months to try out new designs, just for them to fail. With 3D printing, new devices can be printed and tested daily, to determine the best device for implementing µFFIEF in a fraction of the time.

5.2.2 Mass Spectrometry Coupling

As presented in Chapter 5, there is promise in the work for coupling a µFFE device to MALDI-TOF/TOF analysis. Work has shown that the open edge of the device does not affect the flow stability or application of the voltage. It has also been shown that the analytes can flow off of the device. Further work is needed in improving this step though. The analytes coming off the device need to be more efficiently deposited as they exit the µFFE device. It is anticipated that work needs to be done on the electrode buffer channels to determine the optimum flow in the device, and the separation channel Z dimension reduced as much as possible. Currently, the shallowest channel size achieved in a µFFE device by FDM is 50 µm. It is predicted that the dimension could be improved very slightly still using FDM. Future work could also entail moving to a stereolithography 3D printer that could achieve a smaller channel depth. This would allow for slower flow rates, and easier deposition of analytes from the device. Once this is achieved, through prototyping new device designs using 3D printing, a voltage needs to be applied and the separated analytes deposited on the PVDF membrane. It is predicted that desorption from the PVDF by MALDI-TOF/TOF will not be the limited factor, unless very low concentration samples are desired.

If that is the case, further work will need to be done to alleviate this. This could be overcome by concentrating sample on the PVDF membrane off of the µFFE device, or by improving ionization by adjusting the MALDI matrix composition and application. Utilizing a spray coater to apply the matrix to the PVDF membrane is also predicted to help the uniformity of sample desorption, and possibly increase the ionization yield.

µFFE has been shown to be used for numerous applications, made by several different fabrication techniques. This area of research has largely increased, and with the more attainable, and cost effective fabrication techniques I have developed, I anticipate that these methods will be more widely used as these fabrication techniques are further developed and implemented. I also anticipate with the groundwork I laid down for the introduction of a mass spectrometry coupling, that this device will become highly used in smaller laboratories once implemented. The low cost, ease of use, and possibility of identifying analytes off of a PVDF membrane make this device highly desirable. The use of the PVDF membrane also allows for the sample to be cleaned, stored, and shipped out for analysis. This would allow labs that would never dream of using microfluidics, the possibility to use µFFE devices at a fraction of the typical cost, and without the need for a cleanroom for fabrication, or laser setup for detection.

Bibliography

(1) Hannig, K. Z. *fuer Analytical Chemistry* **1961**, *181*, 244-254.
(2) Barrolier, V. J.; Watzke, E.; Gibian, H. Z. *Naturforshung* **1958**, *13B*, 754.
(3) Hoffstetterkuhn, S.; Kuhn, R.; Wagner, H. *Electrophoresis* **1990**, *11*, 304-309.
(4) Hoffstetterkuhn, S.; Wagner, H. *Electrophoresis* **1990**, *11*, 457-462.
(5) Hoffstetterkuhn, S.; Wagner, H. *Electrophoresis* **1990**, *11*, 451-456.
(6) Clifton, M. J.; Jouve, N.; Debalmann, H.; Sanchez, V. *Electrophoresis* **1990**, *11*, 913-919.
(7) Raymond, D. E.; Manz, A.; Widmer, H. M. *Analytical Chemistry* **1994**, *66*, 2858-2865.
(8) Raymond, D. E.; Manz, A.; Widmer, H. M. *Anal.Chem.* **1996**, *68*, 2515-2522.
(9) Kobayashi, H.; Shimamura, K.; Akaida, T.; Sakano, K.; Tajima, N.; Funazaki, J.; Suzuki, H.; Shinohara, E. *J. Chromatogr. A* **2003**, *990*, 169-178.
(10) Fonslow, B. R.; Bowser, M. T. *Anal. Chem.* **2005**, *77*, 5706-5710.
(11) Fonslow, B. R.; Barocas, V. H.; Bowser, M. T. *Analytical Chemistry* **2006**, *78*, 5369-5374.
(12) Zhang, C. X.; Manz, A. *Anal. Chem.* **2003**, *75*, 5759-5766.
(13) Hannig, K.; Heidrich, H. G. *Free-Flow Electrophoresis: An Important Preparative and Analytical Technique for Biology, Biochemistry, and Diagnostics*; GIT Verlag: Darmstadt, Germany, 1990.
(14) Raymond, D. E.; Manz, A.; Widmer, H. M. *Anal.Chem.* **1994**, *66*, 2858-2865.
(15) Turgeon, R. T.; Bowser, M. T. *Anal. Bioanal.Chem.* **2009**, *394*, 187-198.
(16) Vellaichamy, A.; Tran, J. C.; Catherman, A. D.; Lee, J. E.; Kellie, J. F.; Sweet, S. M. M.; Zamdborg, L.; Thomas, P. M.; Ahlf, D. R.; Durbin, K. R.; Valaskovic, G. A.; Kelleher, N. L. *Anal. Chem.* **2010**, *82*, 1234-1244.
(17) Frost, N. W.; Bowser, M. T. *Lab on a Chip* **2010**, *10*, 1231-1236.
(18) Frost, N. W.; Bowser, M. T. *Lab-on-a-Chip* **2010**, *10*, 1231-1236.
(19) Wen, J.; Wilker, E. W.; Yaffe, M. B.; Jensen, K. F. *Anal. Chem.* **2010**, *82*, 1253-1260.
(20) Bottcher, A.; Schlosser, J.; Kronenberg, F.; Dieplinger, H.; Knipping, G.; Lackner, K. J.; Schmitz, G. *J. Lipid Res.* **2000**, *41*, 905-915.
(21) Roman, M. C.; Brown, P. R. *Anal. Chem.* **1994**, *66*, A86-A94.
(22) **Raymond,** D. E.; M**anz, A.**; W**idmer, H. M.** *Anal. Chem.* **1994**, *66*, 2858-2865.
(23) Kohler, S.; Weilbeer, C.; Howitz, S.; Becker, H.; Volker Beushausend; Belder, D. *Lab-on-a-Chip* **2011**, *11*, 309-314.
(24) Walowski, B.; Huttner, W.; Wackerbarth, H. *Anal. Bioanal. Chem.* **2011**, *401*, 2465-2471.
(25) Jezierski, S.; Gitlin, L.; Nagl, S.; Belder, D. *Anal. Bioanal. Chem.* **2011**, *401*, 2651-2656.
(26) Becker, H.; Kohler, S.; Beushausen, V.; Beckert, E.; Howitz, S.; Belder, D. In *14th International Conference on*

Miniaturized Systems for Chemistry and Life Sciences: Groningen, Netherlands, 2010.
(27) Xu, Y.; Zhang, C.-X.; Janasek, D.; Manz, A. *Lab-on-a-Chip* **2003**, *3*, 224-227.
(28) Fonslow, B. R.; Barocas, V. H.; Bowser, M. T. *Anal. Chem.* **2006**, *78*, 5369-5374.
(29) Kohlheyer, D.; Eijkel, J. C. T.; Schlautmann, S.; van den Berg, A.; Schasfoort, R. B. M. *Anal. Chem.* **2008**, *80*, 4111-4118.
(30) Raymond, D. E.; Manz, A.; Widmer, H. M. *Anal. Chem.* **1996**, *68*, 2515-2522.
(31) Wang, P.; Zhang, L.; Shan, Y.; Cong, Y.; Liang, Y.; Han, B.; Liang, Z.; Zhang, Y. *J. Sep. Sci.* **2010**, *33*, 2039-2044.
(32) Mazereeuw, M.; de Best, C. M.; Tjaden, U. R.; Irth, H.; van der Greef, J. *Anal. Chem.* **2000**, *72*, 3881-3886.
(33) Han, B.; Wang, P. L.; Zhu, G. J.; Zhang, L. H.; Qu, F.; Deng, Y. L.; Zhang, Y. K. *J. Sep. Sci.* **2009**, *32*, 1211-1215.
(34) Albrecht, J. W.; Jensen, K. F. *Electrophoresis* **2006**, *27*, 4960-4969.
(35) Lu, H.; Gaudet, S.; Schmidt, M. A.; Jensen, K. F. *Anal. Chem.* **2004**, *76*, 5705-5712.
(36) Kostal, V.; Fonslow, B. R.; Arriaga, E. A.; Bowser, M. T. *Anal. Chem.* **2009**, *81*, 9267-9273.
(37) Fonslow, B. R.; Bowser, M. T. *Analytical Chemistry* **2008**, *80*, 3182-3189.
(38) Turgeon, R. T.; Fonslow, B. R.; Jing, M.; Bowser, M. T. *Anal. Chem.* **2010**, *82*, 3636-3641.
(39) Jing, M.; Bowser, M. T. *Lab-on-a-Chip* **2011**, *11*, 3703-3709.
(40) Geiger, M.; Frost, N. W.; Bowser, M. T. *Anal. Chem.* **2015**, *86*, 5136-5142.
(41) Geiger, M.; Bowser, M. T. *Analytical Chemistry* **2016**, *88*, 2177-2187.
(42) Dittrich, P. S.; Tachikawa, K.; Manz, A. *Anal. Chem.* **2006**, *78*, 3887-3907.
(43) Turgeon, R. T.; Bowser, M. T. *Analytical and Bioanalytical Chemistry* **2009**, *394*, 187-198.
(44) Chang, C. L.; Xu, G. G.; Bai, Y.; Zhang, C. S.; Li, X. J.; Li, M.; Liu, Y.; Liu, H. W. *Anal. Chem.* **2013**, *85*, 170-176.
(45) Theodoridis, G. A.; Gika, H. G.; Want, E. J.; Wilson, I. D. *Anal. Chim. Acta* **2012**, *711*, 7-16.
(46) Westbrook, J. A.; Yan, J. X.; Wait, R.; Welson, S. Y.; Dunn, M. J. *Electrophoresis* **2001**, *22*, 2865-2871.
(47) Whitehouse, C. M.; Dreyer, R. N.; Yamashita, M.; Fenn, J. B. *Anal. Chem.* **1985**, *57*, 675-679.
(48) Keough, T.; Takigiku, R.; Lacey, M. P.; Purdon, M. *Anal. Chem.* **1992**, *64*, 1594-1600.
(49) Verpoorte, E.; De Rooij, N. F. *Proceedings of the Ieee* **2003**, *91*, 930-953.
(50) Fonslow, B. R.; Bowser, M. T. *Anal.Chem.* **2006**, *78*, 8236-8244.
(51) Becker, H.; Locascio, L. E. *Talanta* **2002**, 267-287.
(52) Gartner, C.; Becker, H. *Anall Bioanal Chem* **2008**, *390*, 89-111.

(53) Waldbaur, A.; Rapp, H.; Lange, K.; Rapp, B. E. *Analytical Methods* **2011**, *3*, 2663-2954.
(54) Pereira de Jesus, D.; Blanes, L.; do Lago, C. L. *Electrophoresis* **2006**, *27*, 4935-4942.
(55) Walowski, B.; Huttner, W.; Wackerbarth, H. *Analytical and Bioanalytical Chemistry* **2011**, *401*, 2465-2471.
(56) Ding, H.; Li, X. Q.; Lv, X. F.; Xu, J. D.; Sun, X.; Zhang, Z. M.; Wang, H. L.; Deng, Y. L. *Analyst* **2012**, *137*, 4482-4489.
(57) Akagi, T.; Kubota, R.; Kobayashi, M.; Ichiki, T. *Japanese Journal of Applied Physics* **2015**, *54*, 5.
(58) Kohler, S.; Benz, C.; Becker, H.; Beckert, E.; Beushausen, V.; Belder, D. *Rsc Advances* **2012**, *2*, 520-525.
(59) Huang, T.; Leu, M. C.; Mazumder, J.; Donmez, A. *J. Manuf. Sci. Eng* **2015**, *137*, 1-10.
(60) Gross, B. C.; Erkal, J. L.; Lockwood, S. Y.; Chen, C.; Spence, D. M. *Analytical Chemistry* **2014**, *86*, 3240-3253.
(61) Anderson, K. B.; Lockwood, S. Y.; Martin, R. S.; Spence, D. M. *Analytical Chemistry* **2013**, *85*, 5622-5626.
(62) Bishop, G. W.; Satterwhite, J. E.; Bhakta, S.; Kadimisetty, K.; Gillette, K. M.; Chen, E.; Rusling, J. F. *Analyical Chemistry* **2015**.
(63) Snowden, M. E.; King, P. H.; Covington, J. A.; Macpherson, J. V.; Unwin, P. R. *Analytical Chemistry* **2010**, *82*, 3124-3131.
(64) Shallan, A. I.; Smejkal, P.; Corban, M.; Guijt, R. M.; Breadmore, M. C. *Analytical Chemistry* **2014**, *86*, 3124-3130.
(65) Tsao, C. W.; DeVoe, D. L. *Microfluidics and Nanofluidics* **2009**, *6*, 1-16.
(66) Tsao, C.-W.; DeVoe, D. L. *Microfluidics and Nanofluidics* **2009**, *6*, 1-16.
(67) Tsao, C. W.; DeVoe, D. L. *Microfluid. Nanofluid.* **2009**, *6*, 1-16.
(68) Waldbaur, A.; Rapp, H.; Lange, K.; Rapp, B. E. *Anal. Methods* **2011**, *3*, 2663-2954.
(69) Gross, B. C.; Erkal, J. L.; Lockwood, S. Y.; Chen, C.; Spence, D. M. *Anal. Chem.* **2014**, *86*, 3240-3253.
(70) Waheed, S.; Cabot, J. M.; Macdonald, N. P.; Lewis, T.; Guijt, R. M.; Paull, B.; Breadmore, M. C. *Lab on a Chip* **2016**, *16*, 1993-2013.
(71) Ho, C. M. B.; Ng, S. H.; Li, K. H. H.; Yoon, Y. J. *Lab on a Chip* **2015**, *15*, 3627-3637.
(72) Yazdi, A. A.; Popma, A.; Wong, W.; Nguyen, T.; Pan, Y. Y.; Xu, J. *Microfluidics and Nanofluidics* **2016**, *20*, 18.
(73) Amin, R.; Knowlton, S.; Hart, A.; Yenilmez, B.; Ghaderinezhad, F.; Katebifar, S.; Messina, M.; Khademhosseini, A.; Tasoglu, S. *Biofabrication* **2016**, *8*, 022001.
(74) Au, A. K.; Huynh, W.; Horowitz, L. F.; Folch, A. *Angewandte Chemie-International Edition* **2016**, *55*, 3862-3881.
(75) Morgan, A. J. L.; San Jose, L. H.; Jamieson, W. D.; Wymant, J. M.; Song, B.; Stephens, P.; Barrow, D. A.; Castell, O. K. *Plos One* **2016**, *11*, 17.

(76) Bhattacharjee, N.; Urrios, A.; Kanga, S.; Folch, A. *Lab on a Chip* **2016**, *16*, 1720-1742.
(77) Ghosal, S. *Anal. Chem.* **2002**, *74*, 771-775.
(78) Ghosal, S. *Anal. Chem.* **2002**, *74*, 4198-4203.
(79) Geiger, M.; Harstad, R.; Bowser, M. *Anal. Chem.* **2015**, *87*, 11682-11690.
(80) Hjerten, S. *Chromatogr Rev* **1967**, *9*, 122-219.
(81) McCormick, R. M. *Anal. Chem.* **1988**, 2322-2328.
(82) Lauer, H. H.; McManigill, D. *Anal. Chem.* **1986**, *58*, 166-170.
(83) Corradini, D. *J. Chromatogr., Biomed. Appl.* **1997**, *399*, 221-256.
(84) Verzola, B.; Gelfi, C.; Righetti, P. G. *J. Chromatogr. A* **2000**, *874*, 293-303.
(85) Charles A. Lucy; MacDonald, A. M.; Gulcev, M. D. *J. Chromatogr. A* **2008**, *1184*, 81-405.
(86) Redman, E. A.; Batz , N. G.; Mellors, J. S.; Ramsey, J. M. *Anal. Chem.* **2015**, *87*, 2264-2272.
(87) Jezierski, S.; Belder, D.; Nagl, S. *Chem. Commun.* **2013**, *49*, 904-906.
(88) Osiri, J. K.; Shadpour, H.; Park, S.; Snowden, B. C.; Chen, Z.-Y.; Soper, S. A. *Electrophoresis* **2008**, *29*, 4984-4992.
(89) Lazar, I. M.; Kabulski, J. L. *Lab-on-a-Chip* **2013**, *13*, 2055-2065.
(90) Shallan, A. I.; Smejkal, P.; Corban, M.; Guijt, R. M.; Breadmore, M. C. *Anal. Chem.* **2014**, *86*, 3124-3130.
(91) Fonslow, B. R.; Bowser, M. T. *Anal. Chem.* **2006**, *78*, 8236-8244.
(92) Carrilho, E.; Lunte, S.; Coltro, W. *Electrophoresis* **2008**, *29*, 4928-4937.
(93) Whitesides, G.; Schueller, O.; McDonald, J.; Duffy, D. *Anal. Chem.* **1998**, *70*, 4974-4984.
(94) Anciaux, S. K.; Geiger, M.; Bowser, M. T. *Anal. Chem*.
(95) Verzola, B.; Gelfi, C.; Righetti, P. G. *J. Chromatogr. A* **2000**, *868*, 85-99.
(96) Schomburg, G.; Deege, A.; Köhler, J.; Bien-Vogelsang, U. *J. Chromatogr.* **1983**, *282*, 27-39.
(97) Köhler, J.; Deege, A.; Schomburg, G. **1984**, *18*, 119-124.
(98) Köhler, J.; Chase, D. B.; Farlee, R. D.; Vega, A. J.; Kirkland, J. J. *J. Chromatogr.* **1986**, *352*, 275-305.
(99) Castelletti, L.; Verzola, B.; Gelfi, C.; Stoyanov, A.; Righetti, P. G. *J. Chromatogr. A* **2000**, *894*, 281-289.
(100) Towns, J. K.; Regnier, F. E. *Anal. Chem.* **1992**, *64*, 2473-2478.
(101) Bidlingmeyer, B. A. *J. Chromatogr. Sci.* **1980**, *18*, 525-539.
(102) Sibarani, J.; Takai, M.; Ishihara, K. *Colloids Surf., B* **2007**, *54*, 88-93.
(103) Wong, I.; Ho, C.-M. *Microfluid. Nanofluid.* **2009**, *7*, 291-306.
(104) Ma, Y.; Dong, J.; Bhattacharjee, S.; Wijeratne, S.; Bruening, M. L.; Baker, G. L. *Langmuir* **2013**, *29*, 2946-2954.
(105) Chen, C.; Mehl, B. T.; Munshi, A. S.; Townsend, A. D.; Spence, D. M.; Martin, R. S. *Anal. Methods* **2016**, *8*, 6005-6012.
(106) Johansson, K. S. *Contact Angle, Wettability and Adhesion*; Utrecht: The Netherlands, 2006.
(107) Anciaux, S. K.; Geiger, M.; Bowser, M. T. *Anal. Chem.* **2016**, *88*, 7675-7682.

(108) Radola, B. J. *Biochim. Biophys. Acta, Protein Struct.* **1973**, *295*, 412-428.
(109) Righetti, P. G.; Caravaggio, T. *J. Chromatogr. A* **1976**, *127*, 1-28.
(110) Mellors, J. S.; Gorbounov, V.; Ramsey, R. S.; Ramsey, J. M. *Anal. Chem.* **2008**, *80*, 6881-6887.
(111) Hoffmann, P.; Häusig, U.; Schulze, P.; Belder, D. *Angew. Chem., Int. Ed. Engl.* **2007**, *46*, 4913-4916.
(112) Lee, J.; Soper, S. A.; Murray, K. K. *Rapid Commun. Mass Spectrom.* **2011**, *25*, 693-699.
(113) Tsao, C. W.; Tao, S.; Chen, C. F.; Liu, J. K.; DeVoe, D. L. *Microfluid. Nanofluid.* **2010**, *8*, 777-787.
(114) Zhang, H. Y.; Caprioli, R. M. *Journal of Mass Spectrometry* **1996**, *31*, 1039-1046.
(115) Benz, C.; Boomhoff, M.; Appun, J.; Schneider, C.; Belder, D. *Angewandte Chemie International Edition* **2015**, *54*, 2766-2770.
(116) Balluff, B.; Schone, C.; Hofler, H.; Walch, A. *Histochemistry and Cell Biology* **2011**, *136*, 227-244.